

Stacked Intelligent Metasurfaces for Multicarrier Cognitive Radio ISAC

Alireza Fadakar, *Graduate Student Member* and Andreas F. Molisch, *Fellow, IEEE*

Abstract—The fusion of cognitive radio (CR) and integrated sensing and communication (ISAC), enabled by stacked intelligent metasurfaces (SIMs), offers a promising path for multifunctional programmable front ends in 6G and beyond. In this paper we propose a novel CR-ISAC framework that leverages an SIM integrated with the secondary base station (SB) to learn and realize optimal beampatterns that simultaneously (i) minimize the Bayesian Cramér-Rao bound (BCRB) for localizing a secondary user equipment (SU) and (ii) limit averaged interference at primary user equipments (PUs) so that spectral efficiency loss is constrained, with the target of at most a few percent degradation. We propose an efficient alternating optimization-based algorithm to obtain the optimal end-to-end transmission response of the SIM for all orthogonal frequency division multiplexing (OFDM) subcarriers. Drawing an analogy between the layered SIM architecture and deep neural networks, we define a beampattern-matching loss, derive analytical gradients for backpropagation, and implement a learning-based optimization of the SIM coefficients using a mini-batch Adam optimizer. A complexity analysis is provided, and extensive numerical experiments are performed to evaluate the proposed CR-ISAC framework. The results show that the proposed SIM coefficient optimization methods attain near-optimal performance in terms of both the SU BCRB localization metric and the PUs average spectral efficiency when the SIM has a sufficient number of layers, and they substantially outperform traditional single-layer reconfigurable intelligent surface (RIS) designs.

Index Terms—Cognitive radio, deep learning, integrated sensing and communication (ISAC), localization, OFDM, reconfigurable intelligent surface (RIS), stacked intelligent metasurface (SIM).

I. INTRODUCTION

Rising mobile traffic and the growing demand for higher wireless data rates have intensified radio-spectrum scarcity, posing a major challenge to the deployment of Sixth generation (6G) and beyond communications [1]–[3]. Cognitive radio (CR) has therefore been widely adopted as an effective solution to mitigate spectrum shortage by enabling secondary wireless systems (SWSs) (consisting of secondary base stations (SBs) and secondary user equipments (SUs)) to opportunistically access licensed bands, provided such access does not cause harmful interference to (typically incumbent) primary wireless systems (PWSs) [4], [5], [6, Chap. 27].

Spectrum sharing is typically classified into three modes: interweave, overlay, and underlay [3], [7], [6, Chap. 27]. In the interweave mode, the SWS opportunistically exploits spectral holes that are temporally unused by the licensed PWS. In

the overlay mode, the SWS obtains access opportunities by assisting the PWS transmission. In the underlay mode, the SWS may transmit concurrently with the PWS provided that the resulting performance degradation in terms of quality-of-service (QoS) at each PWS receiver remains below a predefined threshold. This is often achieved by requiring the interference temperature (IT) to remain below a particular threshold [8]. In this context, beamforming is essential to enhance QoS of SWS communication and sensing while ensuring adequate protection of the PWS by limiting interference. This paper focuses on the underlay mode due to its potential for continuous access and superior spectrum efficiency.

On the other hand, with the rapid evolution of 6G systems, advanced enablers such as integrated sensing and communication (ISAC), reconfigurable intelligent surfaces (RISs), and stacked intelligent metasurfaces (SIMs), among others, have been proposed to enhance certain channel characteristics [9], [10]. In particular, ISAC has recently received significant attention as an efficient solution for delivering joint sensing and communication services while improving spectrum usage [9], [11]. Furthermore, RISs and SIMs can assist ISAC by dynamically shaping channel amplitude and phase components to create favorable links for both communication and sensing tasks [9], [12], [13]. Integrating these technologies with established approaches such as CR can further improve overall 6G network performance [14]. Specifically, an RIS comprises a large number of low-cost, nearly passive reflecting elements with tunable reflection coefficients. Operating in a largely passive mode, RISs can be readily integrated into existing cellular and WiFi infrastructures with minimal power and signaling overhead [14]. These properties have stimulated extensive research on RIS-assisted techniques aimed at improving QoS across a wide range of communication scenarios [9], [15]–[18]. However, most existing studies consider single-layer metasurfaces that provide primarily phase-only control compared to a fully digital array of the same aperture and element count, which is capable of joint amplitude and phase weighting. This limitation reduces the optimization degrees of freedom and prevents RISs from reproducing the full set of beampatterns achievable with fully digital arrays.

These limitations have motivated the recent investigation of SIM hardware [13], [19]–[23]. By stacking multiple programmable transmissive metasurface layers, an SIM realizes a deep neural network (DNN)-like architecture that offers substantially richer signal-processing capabilities than single-layer RIS implementations. Moreover, signal propagation within an SIM is governed by electromagnetics (EM) waves (i.e., effectively at the speed of light), whereas the execution speed of conventional DNNs is constrained by electronic processing

A. Fadakar and A. F. Molisch are with the Ming Hsieh Department of Electrical and Computer Engineering, University of Southern California, Los Angeles, California, USA; E-mail: {fadakarg,molisch}@usc.edu.

This work is supported by the National Science Foundation (Grants 2229535 and 2106602).

hardware and its associated latency. A key distinction between SIMs and conventional DNNs is that SIMs do not employ element-wise nonlinear activation functions, operating instead via cascaded linear electromagnetic layers [10], [24]. Hardware prototypes of SIMs have been demonstrated in [24], [25].

A. Related Works

1) *RIS-aided CR Networks*: In recent years, the integration of RIS into CR systems has been extensively studied [3], [5], [26]–[32]. In [3], a two-timescale resource-allocation framework for RIS-aided CR is proposed to maximize the ergodic rate of the SU subject to an average IT constraint at the primary user equipment (PU) receiver and an average transmit-power constraint at the SU transmitter. The work [26] develops a joint design to strengthen secure transmission for both PUs and SUs in an RIS-assisted CR network in the presence of an eavesdropper. Joint optimization of the SU beamforming vector and the RIS phase-shift matrix has been investigated in [27] and [31], where [27] maximizes the SU achievable rate and [31] minimizes the SU transmit power. To reduce the high computational burden of conventional optimization, [28] proposes a deep reinforcement learning (DRL) approach to maximize the SU rate in RIS-assisted CR systems. Robust secure beamforming for millimeter-wave (mmWave) RIS-aided CR is developed in [32], targeting the maximization of the worst-case secrecy rate. From the spectrum sensing (SS) perspective, [29] maximizes the cooperative detection probability in RIS-enabled sensing networks to improve sensing performance. Furthermore, [30] addresses practical hardware impairments and formulates a design that maximizes the average achievable sum rate in multiuser RIS-aided CR systems. Finally, in [5], mobile-sensor signal to interference and noise ratio (SINR) values are maximized via joint optimization of the SS time, SB beamforming, and RIS beamforming, subject to SS and secondary-transmission constraints.

2) *RIS- and SIM-aided Localization and Sensing*: Recent studies have investigated RIS-assisted localization [9], [16]–[18]. In [16], a codebook-based joint localization and synchronization scheme is developed by jointly optimizing the base station (BS) active precoder and the RIS passive phase profiles. The approach in [17] proposes a two-stage, low-complexity solution for joint localization and synchronization using multiple RISs, where a deep-learning-based angle-of-departure (AOD) estimator is employed in the first stage. The works in [9], [18] consider joint estimation of the user equipment (UE) position and mutual-coupling coefficients in multipath environments, addressing the far-field and near-field cases, respectively.

Wireless sensing using SIMs has recently attracted interest [10], [33], [34]. In [10], an SIM is exploited for uplink angle-of-arrival (AOA) estimation by configuring the stacked metasurfaces to implement a 2D discrete Fourier transform (DFT) on the incident field. As waves propagate through the SIM, the receiver array directly observes the angular spectrum, and AOA is estimated by probing the resulting energy distribution across the array. In [33], the BS beamformer and the SIM's end-to-end transmission matrix are jointly optimized to

estimate the complete target-response matrix, while satisfying minimum SINR at communication users and transmit-power limits. Furthermore, [34] proposes a transmit-beamforming design for ISAC using a SIM by performing beamforming in the passive wave domain, which reduces hardware complexity and power consumption.

3) *Gaps and Motivation*: The major gaps in the existing literature can be summarized as follows:

- Although the benefits of RIS in CR networks have been demonstrated [3], [5], [26]–[32], the existing works are mostly communication-centric and ISAC applications within CR particularly localization remain underexplored.
- Current SIM research is predominantly single-functional, focusing on either communication or sensing, and thus the potential of SIMs for multi-functional tasks such as ISAC, localization, and CR has received little attention.
- Algorithmic and beamforming solutions developed for single-layer RIS do not generalize to multi-layer SIM architectures. In particular, to the best of the authors' knowledge, the advantages of SIMs in CR has not yet been studied, motivating the development of novel SIM-specific algorithms and designs.

Motivated by these gaps, this paper studies a multicarrier wideband CR-ISAC system under the underlay scenario and optimizes the SIM coefficients to maximize SU localization performance while ensuring the average IT at PUs remains below a predefined threshold at each orthogonal frequency division multiplexing (OFDM) subcarrier.

B. Contributions

The main contributions of this paper are summarized as follows:

- We study a CR-ISAC system in a wideband OFDM scenario assisted by a multi-functional SIM. Specifically, we formulate an optimization problem to design the SIM coefficients that maximize SU downlink localization performance while satisfying QoS requirement imposed on the PUs.
- We derive the Fisher information matrix (FIM) for the downlink observations and obtain the corresponding Bayesian Cramér-Rao bound (BCRB) assuming a prior on the SU position. The BCRB is then used as the localization metric to design the SIM coefficients.
- We formulate the SIM-coefficient design as an optimization problem that minimizes the BCRB of the SU position, subject to a constraint that the average spectral efficiency (SE) degradation at the PUs does not exceed a predefined threshold. The resulting nonconvex problem is converted to a tractable max-min problem via convex optimization techniques.
- We develop an efficient alternating optimization (AO)-based algorithm to solve the max-min reformulation and obtain the optimal end-to-end transmission response of the SIM for all OFDM subcarriers. Specifically, the inner minimization is solved via a bisection-based method, while a closed-form solution is derived for the outer maximization.

- Exploiting the analogy between SIM architectures and DNNs, we first derive the analytical gradients required for backpropagation and then propose a learning-based scheme that uses the Adam optimizer to tune the SIM coefficients. A beam pattern-based loss function is defined to drive the learned end-to-end response toward the previously obtained optimal solution. Extensive simulations demonstrate convergence of the proposed algorithms and the training procedure. Moreover, the effectiveness of the proposed methods are validated for SU localization, IT management, or equivalently preservation of average SE at the PUs.

Notation: Throughout this paper, boldface uppercase letters (e.g., \mathbf{X}) denote matrices and boldface lowercase letters (e.g., \mathbf{x}) denote vectors; the superscripts $(\cdot)^T$, $(\cdot)^H$, and $(\cdot)^{-1}$ indicate transpose, Hermitian (conjugate transpose), and matrix inverse, respectively. We use $\Re\{\cdot\}$ and $\Im\{\cdot\}$ to denote the real and imaginary parts of a complex-valued quantity, respectively. Horizontal concatenation is written as $[\mathbf{x}_1, \dots, \mathbf{x}_n]$, $\text{diag}(\mathbf{x})$ denotes the diagonal matrix whose main diagonal entries are those of \mathbf{x} , and \mathbf{I}_n is the $n \times n$ identity matrix. We use $\|\mathbf{x}\|$ for the Euclidean norm and $\|\mathbf{A}\|_F$ for the Frobenius norm. $\mathbf{A} \odot \mathbf{B}$ and $\mathbf{A} \otimes \mathbf{B}$ denote the Hadamard and Kronecker products, respectively. The function $\arctan2(x, y)$ refers to the four-quadrant inverse tangent that returns the principal angle of the point (x, y) in $(-\pi, \pi]$. For a real vector $\mathbf{x} = [x_1, \dots, x_n]^T$, $e^{\mathbf{x}}$ denotes the elementwise exponential $[e^{x_1}, \dots, e^{x_n}]^T$. The inner product between two matrices is written as $\mathbf{A} \bullet \mathbf{B} = \text{tr}(\mathbf{A}^H \mathbf{B})$. Finally, $\lambda_{\max}(\mathbf{A})$ denotes the largest eigenvalue of \mathbf{A} .

II. SYSTEM MODEL

The CR-ISAC architecture under study is illustrated in Fig. 1. A single-antenna primary base station (PB) serves N_{pu} single-antenna PUs¹ in the downlink, while a single-antenna SB integrated with an SIM, thus creating a reconfigurable antenna, simultaneously provides sensing via dedicated downlink pilot transmissions for SUs while keeping the average SE of the PUs above a threshold. We assume that the relevant channel state information (CSI) namely, the PB-PUs and SB-PUs channels have been estimated and exchanged over a coordinated CR control unit [5].

The SB emits I OFDM downlink symbols through the SIM for localizing a single-antenna SU. Moreover, the SIM is connected to a smart controller, such as a customized field-programmable gate array (FPGA), which is capable of independently adjusting the phase shift of the EM waves transmitted through each meta-atom [12]. Our goal is to optimize the SIM phase coefficients so as to maximize localization performance, while keeping the resulting interference leakage to the PUs under a specific limit. Because the downlink localization procedure can be carried out independently at each SU, in this paper we focus on the single SU case without loss of generality.

¹The choice of a single-antenna PB and PUs is made solely for notational simplicity and exposition. No assumptions are imposed on the internal structure of the PWS. Extension of the PWS components to multi-antenna architectures is straightforward and does not alter the proposed methodologies.

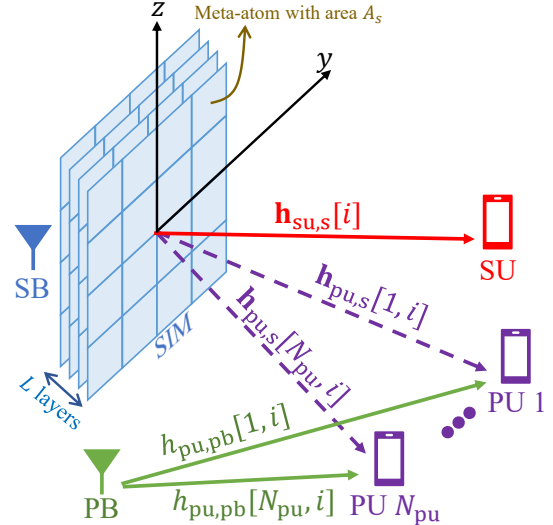


Fig. 1: The considered SIM-aided CR-ISAC system. We aim to optimize the SIM coefficients to maximize the localization performance at the SU while keeping the averaged SE at the PUs above a threshold.

A. Signal Model

1) *SIM Signal Models:* The considered SIM consists of an array of L metasurfaces, each having a uniform planar array (UPA) shaped containing $N = N^h N^v$ meta-atoms with N^h rows and N^v columns. The phase shift matrix for the ℓ -th SIM layer is denoted by

$$\Phi^{(\ell)} = \text{diag}([e^{j\phi_1^{(\ell)}}, \dots, e^{j\phi_N^{(\ell)}}]^T) \in \mathbb{C}^{N \times N}, \quad (1)$$

where $\phi_n^{(\ell)}$ denotes the phase shift of the n -th meta-atom on the ℓ -th metasurface layer. For $\ell = 2, \dots, L$, let $\mathbf{W}^{(\ell)}[i] \in \mathbb{C}^{N \times N}$ represent the transmission matrix from the $(\ell - 1)$ -th to the ℓ -th metasurface layer in the i -th subcarrier. According to the Rayleigh-Sommerfeld diffraction theory, the (n, n') -th entry of the wideband transmission matrix of the SIM is expressed as [10], [12], [20]:

$$[\mathbf{W}^{(\ell)}[i]]_{n,n'} = \frac{A_s d_s}{(d_{n,n'}^{(\ell)})^2} \left(\frac{1}{2\pi d_{n,n'}^{(\ell)}} - j \frac{f_i}{c} \right) e^{j2\pi d_{n,n'}^{(\ell)} f_i / c}, \quad (2)$$

where A_s is the area of each meta-atom, d_s is the inter-layer distance in the SIM, $f_i = f_c - (i - 1)\Delta f$ is the frequency of the i -th subcarrier (with f_c the carrier frequency and Δf the subcarrier spacing), and c is the speed of light. The inter-layer distance between the n -th meta-atom of the ℓ -th layer and the n' -th meta-atom of the $(\ell - 1)$ -th layer is represented as $d_{n,n'}^{(\ell)}$. Finally, the cumulative effect of signal propagation through the layers of the SIM in the i -th subcarrier is characterized by $\mathbf{G}[i] \in \mathbb{C}^{N \times N}$ obtained as [12], [35]:

$$\mathbf{G}[i] = \Phi^{(L)} \mathbf{W}^{(L)}[i] \dots \Phi^{(2)} \mathbf{W}^{(2)}[i] \Phi^{(1)}. \quad (3)$$

2) *Received Downlink Signal Models:* The received signal at the SU and the r -th PU over the i -th subcarrier are given by:

$$y_{\text{su}}[i] = \sqrt{P_{\text{sb}}} \mathbf{h}_{\text{su,s}}^T[i] \mathbf{G}[i] \mathbf{w}[i] + v_{\text{su}}[i], \quad (4a)$$

$$y_{\text{pu}}[r, i] = \sqrt{P_{\text{pb}}} h_{\text{pu,pb}}[r, i] s[r, i] + \sqrt{P_{\text{sb}}} \mathbf{h}_{\text{pu,s}}[r, i]^T \mathbf{G}[i] \mathbf{w}[i] + v_{\text{pu}}[r, i], \quad (4b)$$

where $\mathbf{w}[i] \in \mathbb{C}^N$ is the transmission vector from the SB to the first layer of the SIM. Moreover, P_{sb} and P_{pb} represent the total transmitted power from the SB and PB, respectively. The

communication symbol transmitted from the PB to the r -th PU in the i -th subcarrier is denoted by $s[r, i]$, which satisfies the unit-power condition $\mathbb{E}[|s[r, i]|^2] = 1$. $v_{\text{su}}[i] \sim \mathcal{CN}(0, \sigma^2)$ denotes the joint contribution of the additive white Gaussian noise (AWGN) and the interference from the PB at the SU, and $v_{\text{pu}}[r, i] \sim \mathcal{CN}(0, \sigma_v^2)$ denote the AWGN at the r -th PU. Additionally, $\mathbf{h}_{\text{su,s}}[i] \in \mathbb{C}^N$, $h_{\text{pu,pb}}[r, i] \in \mathbb{C}$, and $\mathbf{h}_{\text{pu,s}}[r, i] \in \mathbb{C}^N$ denote the SU-SIM, PU-PB, and PU-SIM channels, respectively which will be explained in detail in the following subsection.

B. Channel Model

A widely used approach for representing the wideband OFDM channel model is the frequency-domain form, which simplifies beamspace processing via the IFFT/FFT [35], [36]. Assuming a block-fading geometric channel model [37], [38] between any two components of the considered CR-ISAC system, the channels are modeled as follows:

$$\mathbf{h}_{\text{su,s}}[i] = \bar{\mathbf{h}}_{\text{su,s}}[i] + \sum_{q=1}^{Q_{\text{su,s}}} \tilde{\mathbf{h}}_{\text{su,s}}^{(q)}[i], \quad (5a)$$

$$\mathbf{h}_{\text{pu,s}}[r, i] = \bar{\mathbf{h}}_{\text{pu,s}}[r, i] + \sum_{q=1}^{Q_{\text{pu,s}}} \tilde{\mathbf{h}}_{\text{pu,s}}^{(q)}[r, i], \quad (5b)$$

$$h_{\text{pu,pb}}[r, i] = \bar{h}_{\text{pu,pb}}[r, i] + \sum_{q=1}^{Q_{\text{pu,pb}}} \tilde{h}_{\text{pu,pb}}^{(q)}[r, i], \quad (5c)$$

where $\mathbf{h}_{\text{su,s}}[i] \in \mathbb{C}^N$ denotes the channel between the SIM and SU, $\mathbf{h}_{\text{pu,s}}[r, i] \in \mathbb{C}^N$ is the channel between the SIM and the r -th PU, and $h_{\text{pu,pb}}[r, i]$ is the channel between the PB and the r -th PU. The index i corresponds to the i -th subcarrier. Moreover, $\bar{\mathbf{h}}_{\text{su,s}}[i]$, $\bar{\mathbf{h}}_{\text{pu,s}}[r, i]$, and $\bar{h}_{\text{pu,pb}}[r, i]$ denote the line-of-sight (LoS) terms of these channels, respectively. Likewise, $\tilde{\mathbf{h}}_{\text{su,s}}^{(q)}[i]$, $\tilde{\mathbf{h}}_{\text{pu,s}}^{(q)}[r, i]$, and $\tilde{h}_{\text{pu,pb}}^{(q)}[r, i]$ represent the non-line-of-sight (NLoS) components through the q -th multipath component (MPC). Finally, $Q_{\text{su,s}}$, $Q_{\text{pu,s}}$, and $Q_{\text{pu,pb}}$ are the number of such NLoS paths in the corresponding channels.

The LoS terms of the channels are defined as follows:

$$\bar{\mathbf{h}}_{\text{su,s}}[i] = \alpha_{\text{su,s}} e^{-j\zeta_i \tau_{\text{su,s}}} \mathbf{a}_i(\boldsymbol{\theta}_{\text{su,s}}), \quad (6a)$$

$$\bar{\mathbf{h}}_{\text{pu,s}}[r, i] = \alpha_{\text{pu,s}}[r] e^{-j\zeta_i \tau_{\text{pu,s}}[r]} \mathbf{a}_i(\boldsymbol{\theta}_{\text{pu,s}}[r]), \quad (6b)$$

$$\bar{h}_{\text{pu,pb}}[r, i] = \alpha_{\text{pu,pb}}[r] e^{-j\zeta_i \tau_{\text{pu,pb}}[r]}, \quad (6c)$$

where $\alpha_{\text{su,s}}$, $\alpha_{\text{pu,s}}[r]$, and $\alpha_{\text{pu,pb}}[r, i]$ denote the corresponding overall complex gain of the channels. In addition, $\zeta_i = 2\pi(i-1)\Delta f$, and the delay $\tau_{u,v}$ between two components u, v is defined as $\tau_{u,v} = \|\mathbf{p}_u - \mathbf{p}_v\|/c$. In (6), $\boldsymbol{\theta}_{\text{su,s}} = [\theta_{\text{su,s}}^{\text{el}}, \theta_{\text{su,s}}^{\text{az}}]^T$ and $\boldsymbol{\theta}_{\text{pu,s}}[r] = [\theta_{\text{pu,s}}^{\text{el}}[r], \theta_{\text{pu,s}}^{\text{az}}[r]]^T$ denote the 2D-AOD from the last layer of the SIM towards the the SU and the r -th PU, respectively. The angles $\theta_{\text{su,s}}^{\text{el}}$, $\theta_{\text{su,s}}^{\text{az}}$ are related to the positions of these components as follows:

$$\theta_{\text{su,s}}^{\text{el}} = \arccos\left(\frac{[\mathbf{p}_{\text{su,s}}]_3}{\|\mathbf{p}_{\text{su,s}}\|}\right), \quad \theta_{\text{su,s}}^{\text{az}} = \arctan2([\mathbf{p}_{\text{su,s}}]_2, [\mathbf{p}_{\text{su,s}}]_1), \quad (7)$$

where $\mathbf{p}_{\text{su,s}} = \mathbf{R}_s^T(\mathbf{p}_{\text{su}} - \mathbf{p}_s)$ denotes the local coordinates of \mathbf{p}_{su} with respect to the SIM. Similar equations can be obtained for $\theta_{\text{pu,s}}^{\text{el}}[r]$, $\theta_{\text{pu,s}}^{\text{az}}[r]$. The array response vector (ARV) of the last

layer of the SIM at the i -th subcarrier, denoted by $\mathbf{a}_i(\boldsymbol{\theta})$, is defined as:

$$\mathbf{a}_i(\boldsymbol{\theta}) = e^{-j2\pi\omega_i^h \mathbf{k}(N^h)} \otimes e^{-j2\pi\omega_i^v \mathbf{k}(N^v)}, \quad (8)$$

where $\mathbf{k}(N) = [0, \dots, N-1]^T$, and ω_i^h and ω_i^v represent the spatial horizontal and vertical frequencies for the i -th subcarrier, respectively. As shown in Fig. 1, if the SIM UPA-shaped layers are positioned parallel to the y - z plane of the local Cartesian coordinate system of the SB, then

$$\omega_i^h = d \sin(\theta^{\text{az}}) \sin(\theta^{\text{el}})/\lambda_i, \quad \omega_i^v = d \cos(\theta^{\text{el}})/\lambda_i, \quad (9)$$

where d , denotes the distance between two adjacent meta-atoms in each SIM layer, and $\lambda_i = c/f_i$ is the wavelength of the i -th subcarrier frequency. Moreover, θ^{az} , θ^{el} represent the azimuth and elevation angles in the SB's local Cartesian coordinates. Azimuth $\theta^{\text{az}} \in [-\pi, \pi]$ is measured from $+y$ toward $+x$, and elevation $\theta^{\text{el}} \in [0, \pi]$ is the angle with respect to $+z$ direction. All parameters associated with the NLoS paths in (5) are defined in a similar manner using single-point scatterers. To focus on the main tasks of the paper, we assume that the channels at the PUs i.e., $h_{\text{pu,pb}}[r, i]$ and $\mathbf{h}_{\text{pu,s}}[r, i]$ are estimated and known at the SB for the design of the SIM phase coefficients.

III. LOWER BOUND ANALYSIS AND PROBLEM FORMULATION

In this section, we perform FIM analysis to derive the Cramér-Rao bound (CRB) values for the channel and state parameters, which play a crucial role in designing the SIM phase coefficients. Note that the NLoS components via the MPCs in the SU-SIM channel of (5a) do not contribute to the theoretical localizability of the SU [9], [39], [40], and they may degrade performance by producing unresolvable paths. Accordingly, the lower bounds presented in this paper are derived only considering the LoS path between the SIM and the SU, rather than the full model in (4a), (5a).

1) *CRB in Channel Domain*: In this subsection, we compute the standard FIM of the unknown channel parameter vector $\boldsymbol{\eta} = [\theta_{\text{su,s}}^{\text{el}}, \theta_{\text{su,s}}^{\text{az}}, \tau_{\text{su,s}}, \rho_{\text{su,s}}, \varphi_{\text{su,s}}]^T$ where $\rho_{\text{su,s}}$, $\varphi_{\text{su,s}}$ are the magnitude and phase components of the complex path gain $\alpha_{\text{su,s}}$. Since the observations in (4a) are complex Gaussian, we utilize Slepian-Bangs formula to obtain the FIM $\mathbf{J}_{\boldsymbol{\eta}} \in \mathbb{R}^{5 \times 5}$ [16], [40]. Specifically, the (u, w) -th element can be computed as:

$$[\mathbf{J}_{\boldsymbol{\eta}}]_{u,w} = \frac{2}{\sigma^2} \sum_{i=1}^I \Re \left\{ \left(\frac{\partial x_{\text{su}}[i]}{\partial [\boldsymbol{\eta}]_u} \right)^* \left(\frac{\partial x_{\text{su}}[i]}{\partial [\boldsymbol{\eta}]_w} \right) \right\}, \quad (10)$$

where $x_{\text{su}}[i]$ denotes the noise- and multipath-free component of (4a), which can be represented as:

$$x_{\text{su}}[i] = \mathbf{c}[i]^T \mathbf{f}[i], \quad (11)$$

where $\mathbf{f}[i] \in \mathbb{C}^N$ is the tunable end-to-end response of the SIM in the i -th subcarrier:

$$\mathbf{f}[i] = \mathbf{G}[i] \mathbf{w}[i], \quad (12)$$

and $\mathbf{c}[i] \in \mathbb{C}^N$ is an uncontrollable vector proportional to the LoS channel, are defined as follows:

$$\mathbf{c}[i] = \sqrt{P_{\text{sb}}} \bar{\mathbf{h}}_{\text{su,s}}[i] = \sqrt{P_{\text{sb}}} \alpha_{\text{su,s}} e^{-j\zeta_i \tau_{\text{su,s}}} \mathbf{a}_i(\boldsymbol{\theta}_{\text{su,s}}). \quad (13)$$

Thus, the FIM entries in (10) can be represented as:

$$[\mathbf{J}_{\boldsymbol{\eta}}]_{u,w} = \frac{2}{\sigma^2} \sum_{i=1}^I \Re \{ \mathbf{f}[i]^H \mathbf{c}_u[i]^* \mathbf{c}_w[i]^T \mathbf{f}[i] \}, \quad (14)$$

where $\mathbf{c}_u = \partial \mathbf{c} / \partial [\boldsymbol{\eta}]_u$.

2) *CRB in State Domain*: To obtain the FIM $\mathbf{J}_\gamma \in \mathbb{R}^{5 \times 5}$ for the state domain vector $\gamma = [\mathbf{p}_{\text{su}}^\top, \rho_{\text{su,s}}, \varphi_{\text{su,s}}]^\top$, we use the Jacobian transformation matrix $\mathbf{T} = \frac{\partial \boldsymbol{\eta}^\top}{\partial \boldsymbol{\gamma}} \in \mathbb{R}^{5 \times 5}$ as $\mathbf{J}_\gamma = \mathbf{T} \mathbf{J}_\eta \mathbf{T}^\top$. Thus, using (14), the (u, w) -th element of \mathbf{J}_γ can be represented as:

$$[\mathbf{J}_\gamma]_{u,w} = \frac{2}{\sigma^2} \sum_{i=1}^I \Re \{ \mathbf{f}[i]^\text{H} \tilde{\mathbf{c}}_u[i]^* \tilde{\mathbf{c}}_w[i]^\text{T} \mathbf{f}[i] \} \quad (15)$$

where

$$\tilde{\mathbf{c}}_u[i] = \sum_{j=1}^5 [\mathbf{T}]_{u,j} \mathbf{c}_j[i]. \quad (16)$$

3) *Bayesian CRB in State Domain*: Assuming a prior probability density function (PDF) $p(\gamma) \in \mathbb{R}^5$ for the state parameter vector γ , the Bayesian Fisher information matrix (BFIM) is defined as follows:

$$\mathbf{J}_B = \mathbf{J}_D + \mathbf{J}_P, \quad (17)$$

where

$$\mathbf{J}_D = \mathbb{E}_\gamma [\mathbf{J}_\gamma(\gamma)], \quad (18)$$

whose (u, w) -th entry can be obtained by applying expectation on (15):

$$[\mathbf{J}_D]_{u,w} = \sum_{i=1}^I \Re \left\{ \mathbf{f}[i]^\text{H} \mathbb{E}_\gamma \left[\frac{2}{\sigma^2} \tilde{\mathbf{c}}_u^*[i] \tilde{\mathbf{c}}_w^\text{T}[i] \right] \mathbf{f}[i] \right\}, \quad (19)$$

and

$$\mathbf{J}_P = \mathbb{E}_\gamma \left[-\nabla_\gamma^2 \ln p(\gamma) \right], \quad (20)$$

where $\nabla_\gamma^2 \triangleq \frac{\partial^2}{\partial \boldsymbol{\gamma} \partial \boldsymbol{\gamma}^\text{T}}$ denotes the Hessian matrix operator. Finally, the SU position BCRB is defined as:

$$\text{BCRB} = \text{tr}([\mathbf{J}_B^{-1}]_{1:3,1:3}). \quad (21)$$

A. Average SINR at the PUs

The average SINR at the PUs on the i -th subcarrier is defined as:

$$\text{SINR}[i] = \frac{S^2[i]}{I^2[i] + \sigma_v^2}, \quad \overline{\text{SINR}}[i] = \frac{S^2[i]}{\sigma_v^2}, \quad (22)$$

where $\text{SINR}[i]$ denotes the SINR in presence of interference, and $\overline{\text{SINR}}[i]$ represents the same value in absence of the interference from the SIM. Moreover, $S^2[i]$ and $I^2[i]$ denote the average signal and interference power, respectively, at the PUs on the i -th subcarrier, which are given by:

$$S^2[i] = \frac{P_{\text{pb}}}{N_{\text{pu}}} \sum_{r=1}^{N_{\text{pu}}} |h_{\text{pu,pb}}[r, i]|^2 \quad (23)$$

$$I^2[i] = \frac{P_{\text{sb}}}{N_{\text{pu}}} \sum_{r=1}^{N_{\text{pu}}} \|\mathbf{h}_{\text{pu,s}}[i]^\text{T} \mathbf{f}[i]\|^2 = \mathbf{f}[i]^\text{H} \mathbf{R}_{\text{pu}} \mathbf{f}[i], \quad (24)$$

where

$$\mathbf{R}_{\text{pu}}[i] = \frac{P_{\text{sb}}}{N_{\text{pu}}} \sum_{r=1}^{N_{\text{pu}}} \mathbf{h}_{\text{pu,s}}^*[r, i] \mathbf{h}_{\text{pu,s}}[r, i]^\text{T}. \quad (25)$$

B. Problem Formulation

The design of the phase shift coefficients of the SIM layers must simultaneously: (i) minimize the SU BCRB, and (ii) keep the averaged SE of the PUs above a certain threshold. To this end, the optimization problem can be formulated as follows:

$$\min_{\{\boldsymbol{\Phi}^{(\ell)}\}_{\ell=1}^L} \text{BCRB}(\{\boldsymbol{\Phi}^{(\ell)}\}_{\ell=1}^L) \quad (26a)$$

$$\text{s.t. } \log_2(1 + \text{SINR}[i]) \geq \kappa \log_2(1 + \overline{\text{SINR}}[i]), \quad (26b)$$

$$i = 1, \dots, I,$$

$$|\boldsymbol{\Phi}^{(\ell)}|_{n,n} = 1, \quad (26c)$$

$$\forall n = 1, \dots, N, \forall \ell = 1, \dots, L,$$

where (26b) ensures that the average data rate at the PUs is at least κ times the average data rate when SB is not transmitting, and (26c) imposes the unit-modulus constraint on the SIM layer coefficients.

IV. PROPOSED BEAMFORMING METHOD

Problem (26) is non-convex and high-dimensional and challenging due to coupled phase coefficients of the SIM layers. To make the problem tractable, we first assume a full freedom over the end-to-end SIM response vectors $\mathbf{f}[i]$ and drop the condition (12). After optimizing the vectors $\mathbf{f}[i]$, we will optimize the SIM coefficients in Sec. V. Thus, the relaxed problem can be reformulated as follows:

$$\min_{\{\mathbf{f}[i]\}_{i=1}^I} \text{BCRB}(\{\mathbf{f}[i]\}_{i=1}^I) \quad (27a)$$

$$\text{s.t. } \epsilon[i] \geq \mathbf{f}[i]^\text{H} \mathbf{R}_{\text{pu}}[i] \mathbf{f}[i], \quad i = 1, \dots, I, \quad (27b)$$

$$\|\mathbf{f}[i]\|^2 \leq \delta[i], \quad (27c)$$

where (27b) is equivalent to (26b) where $\epsilon[i]$ is defined as:

$$\epsilon[i] = \frac{S^2[i] - R[i]\sigma^2}{R[i]} \quad (28)$$

where $R[i] = (1 + \overline{\text{SINR}}[i])^\kappa - 1$, and, since $\mathbf{f}[i]$ is upper-bounded according to (12), constraint (27c) enforces the per-subcarrier power limit $\delta[i]$ on $\mathbf{f}[i]$.

Proposition 1. *The problem (27) is equivalent to:*

$$\max_{\{\mathbf{d}_j\}_{j=1}^3} \min_{\{\mathbf{f}[i]\}_{i=1}^I} \sum_{j=1}^3 (-\mathbf{d}_j^\text{T} \mathbf{J}_B \mathbf{d}_j + 2\mathbf{d}_j^\text{T} \mathbf{e}_j) \quad (29a)$$

$$\text{s.t. } (27b), (27c),$$

where $\mathbf{d}_j \in \mathbb{R}^5$ for $j = 1, 2, 3$ are optimization variables for the outer maximization subproblem. This problem can be also represented as:

$$\max_{\{\mathbf{d}_j\}_{j=1}^3} \min_{\{\mathbf{f}[i]\}_{i=1}^I} \left[\sum_{j=1}^3 (-\mathbf{d}_j^\text{T} \mathbf{J}_P \mathbf{d}_j + 2\mathbf{d}_j^\text{T} \mathbf{e}_j) - \sum_{i=1}^I \Re \{ \mathbf{f}[i]^\text{H} \overline{\mathbf{C}}[i] \mathbf{f}[i] \} \right] \quad (30a)$$

$$\text{s.t. } (27b), (27c),$$

where \mathbf{e}_j is the j -th column of the identity matrix \mathbf{I}_5 and:

$$\overline{\mathbf{C}}[i] = \sum_{j=1}^3 \mathbb{E} \left[\frac{2}{\sigma^2} \bar{\mathbf{c}}_{\mathbf{d}_j}[i]^* \bar{\mathbf{c}}_{\mathbf{d}_j}[i]^\text{T} \right] \quad (31)$$

where

$$\bar{\mathbf{c}}_{\mathbf{d}_j}[i] = \sum_{r=1}^5 [\mathbf{d}_j]_r \tilde{\mathbf{c}}_r[i] \quad (32)$$

Proof. See Appendix A.

Hence, in order to solve the original problem (26), we first solve the equivalent problem (29) or (30), and then we optimize the SIM's coefficients in the next section. To tackle the max-min problem (29), we resort to AO algorithm to iteratively solve the inner min and outer max problems until convergence whose details are explained next.

A. Inner Optimization

For any subcarrier index i , the optimal vector $\hat{\mathbf{f}}[i]$ can be obtained using the following proposition:

Proposition 2. *Since for each subcarrier the inner optimization problem in (30) is solved independently from other subcarriers, we drop the subcarrier index i for notational simplicity. Let $\mathbf{A} = \frac{1}{2}(\overline{\mathbf{C}} + \overline{\mathbf{C}}^H)$. Then, assuming fixed vectors $\{\mathbf{d}_j\}_{j=1}^3$, the optimal solution to the inner optimization can be obtained using Algorithm 1.*

Proof. See Appendix B.

Algorithm 1 Proposed Method for the Inner Optimization (30)

- 1: **Inputs:** Matrix $\mathbf{A} = \frac{1}{2}(\overline{\mathbf{C}} + \overline{\mathbf{C}}^H)$, covariance matrix \mathbf{R} , scalars $\kappa, \delta > 0$, and the tolerance $\xi_{\text{tol}} > 0$.
 - 2: Obtain ϵ based on κ using (28).
 - 3: **If** $\lambda_{\max}(\mathbf{A}) \leq 0$ **then return** $\hat{\mathbf{f}} = \mathbf{0}$ **End If**
 - 4: Compute principal unit eigenvector \mathbf{u} of \mathbf{A} .
 - 5: **If** $\mathbf{u}^H \mathbf{R} \mathbf{u} \leq \epsilon/\delta$ **then return** $\hat{\mathbf{f}} = \sqrt{\delta} \mathbf{u}$.
 - 6: **Else** We need to find $\mu > 0$ s.t. $g(\mu) \triangleq \mathbf{v}(\mu)^H \mathbf{R} \mathbf{v}(\mu) = \epsilon/\delta$ where $\mathbf{v}(\mu)$ is the principal eigenvector of $\mathbf{A} - \mu \mathbf{R}$
 - 7: **Perform bisection algorithm to find** μ :
 - 8: $\mu_\ell \leftarrow 0, \mu_u \leftarrow 1$
 - 9: **While** $g(\mu_u) > \epsilon/\delta$ **do** $\mu_u \leftarrow 2\mu_u$ **end while**
 - 10: **repeat**
 - 11: $\mu \leftarrow (\mu_\ell + \mu_u)/2$
 - 12: compute principal unit eigenvector $\mathbf{v}(\mu)$ of $\mathbf{A} - \mu \mathbf{R}$
 - 13: $g(\mu) \leftarrow \mathbf{v}(\mu)^H \mathbf{R} \mathbf{v}(\mu)$
 - 14: **If** $g(\mu) > \epsilon/\delta$ **then** $\mu_\ell \leftarrow \mu$ **else** $\mu_u \leftarrow \mu$ **end if**
 - 15: **until** $|g(\mu) - \epsilon/\delta| < \xi_{\text{tol}}$
 - 16: **Output:** $\hat{\mathbf{f}} = \sqrt{\delta} \mathbf{v}(\mu)$.
-

B. Outer Optimization

Assuming fixed vectors $\{\hat{\mathbf{f}}[i]\}_{i=1}^I$, the outer maximization problem in (29) can be represented as:

$$\max_{\{\mathbf{d}_j\}_{j=1}^3} \sum_{j=1}^3 \left(-\mathbf{d}_j^T \mathbf{J}_B \mathbf{d}_j + 2 \mathbf{e}_j^T \mathbf{d}_j \right). \quad (33)$$

Proposition 3. *The problem (33) can be solved independently for each $j = 1, 2, 3$, and each $\mathbf{d}_j \in \mathbb{R}^5$ is uniquely obtained as:*

$$\hat{\mathbf{d}}_j = \mathbf{J}_B^{-1} \mathbf{e}_j, \quad j = 1, 2, 3. \quad (34)$$

Proof. See Appendix C.

C. Alternating optimization

In the previous subsections, we solved the inner and outer optimization subproblems in the max-min problem (29) independently. In this subsection we propose an AO based algorithm to solve the entire problem. To this end, we iteratively optimize the vectors $\{\hat{\mathbf{f}}[i]\}_{i=1}^I$ and $\{\mathbf{d}_j\}_{j=1}^3$ using Algorithm 1 and (34), respectively until convergence. Details are provided in Algorithm 2. Note that in Prop. 2 we solved the problem

using fixed vectors $\{\mathbf{d}_j\}_{j=1}^3$. Thus, it is essential to obtain a robust initialization for these vectors. First, we provide the following lemma:

Lemma 1. *A lower bound for BCRB can be obtained as:*

$$\text{BCRB} \geq \frac{9}{\text{tr}([\mathbf{J}_B]_{1:3,1:3})}. \quad (35)$$

Proof. See Appendix D.

From Lemma 1, it can be seen that $9/\text{tr}([\mathbf{J}_B]_{1:3,1:3})$ is a lower bound for the BCRB. Hence, maximizing $\text{tr}([\mathbf{J}_B]_{1:3,1:3})$ would minimize this lower bound. Note that:

$$\text{tr}([\mathbf{J}_B]_{1:3,1:3}) = \sum_{j=1}^3 \mathbf{e}_j^T \mathbf{J}_B \mathbf{e}_j. \quad (36)$$

Comparing (36) with (29a), we observe that (36) is the objective value of the inner optimization problem using the vectors $\mathbf{d}_j = \mathbf{e}_j$ for $j \in \{1, 2, 3\}$. Hence, the vector \mathbf{e}_j is a suitable choice as initialization for the vector \mathbf{d}_j .

Algorithm 2 Alternating optimization to solve (29)

- 1: **Inputs:** tolerances $\epsilon_{\text{tol}}, \tau_{\text{tol}}$.
 - 2: **Initialization:** $\mathbf{d}_j \leftarrow \mathbf{e}_j$ for $j \in \{1, 2, 3\}$, $\mathbf{D}^{(0)} = [\mathbf{d}_1, \mathbf{d}_2, \mathbf{d}_3]$, $g^{(0)} \leftarrow \infty$.
 - 3: **while** $|g^{(k)} - g^{(k-1)}|/|g^{(k-1)}| > \epsilon_{\text{tol}}$ **and** $\|\mathbf{D}^{(k)} - \mathbf{D}^{(k-1)}\|_F > \tau_{\text{tol}}$ **do**
 - 4: Update $\{\hat{\mathbf{f}}[i]\}_{i=1}^I$ via Algorithm 1.
 $g^{(k)} \leftarrow$ objective value (29a).
 - 5: Update $\{\mathbf{d}_j\}_{j=1}^3$ based on closed form solution (34).
 $\mathbf{D}^{(k)} \leftarrow [\mathbf{d}_1, \mathbf{d}_2, \mathbf{d}_3]$.
 - 6: **end while**
 - 7: **Outputs:** $\{\hat{\mathbf{f}}[i]\}_{i=1}^I$, $\{\hat{\mathbf{d}}_j\}_{j=1}^3$
-

V. OPTIMIZATION OF THE SIM COEFFICIENTS

In Sec. IV, the vectors $\hat{\mathbf{f}}[i]$ are optimized for each subcarrier index $i \in \{1, \dots, I\}$ without considering the key equation (12) which establishes the connection between $\hat{\mathbf{f}}[i]$ and the SIM's propagation matrix $\mathbf{G}[i]$ (defined in (3)). In the rest of this section, we denote these optimized vectors as $\hat{\mathbf{f}}[i]$ (i.e., the outputs of Algorithm 2). Observing the signal models in (4a) and (6a), to optimize the SIM's phase coefficients, we try to choose the phase shifts to achieve the most similar beampatterns obtained by $\{\hat{\mathbf{f}}[i]\}_{i=1}^I$. Thus, the problem can be formulated as follows:

$$\min_{\{\Phi^{(i)}\}_{i=1}^I} \frac{1}{I} \sum_{i=1}^I \|\mathbf{b}[i] - \mathbf{q}[i]\|^2, \quad \text{s.t. } \mathbf{b}[i] = \mathbf{A}[i]^T \mathbf{G}[i] \mathbf{w}[i], \quad (37)$$

where $\mathbf{q}[i] = \mathbf{A}[i]^T \hat{\mathbf{f}}[i]$ denotes the beampattern of the vector $\hat{\mathbf{f}}[i]$. $\mathbf{A}[i] = [\mathbf{a}_i(\boldsymbol{\theta}_1), \dots, \mathbf{a}_i(\boldsymbol{\theta}_{N_g})]$, is the collection of ARV at N_g 2D-AOD grids in the i -th subcarrier. To solve (37), and motivated by the structural similarity between (3) and DNNs, we adopt a mini-batch optimization approach. In each batch we evaluate the beampattern-matching loss (37) on a randomly drawn angular grid of size N_g and update the SIM phase coefficients via backpropagation and a gradient-based optimizer. Implementation details are given in the following subsections.

A. Forward and backward recursions

To evaluate $\mathbf{f}[i]$ and to compute gradients efficiently we use right (forward) and left (backward) recursions.

Define right vectors $\mathbf{r}^{(\ell)}[i] \in \mathbb{C}^N$ for layer ℓ and subcarrier i by $\mathbf{r}^{(1)}[i] = \mathbf{w}[i]$, and for $\ell = 2, \dots, L$,

$$\mathbf{r}^{(\ell)}[i] = \mathbf{W}^{(\ell)}[i] (\Phi^{(\ell-1)} \mathbf{r}^{(\ell-1)}[i]). \quad (38)$$

Thus the vector entering layer ℓ (before multiplication by the diagonal phase $\Phi^{(\ell)}$) is $\mathbf{r}^{(\ell)}[i]$. In a similar manner, we define left matrices $\mathbf{L}^{(\ell)}[i] \in \mathbb{C}^{N \times N}$ by $\mathbf{L}^{(L)}[i] = \mathbf{I}_N$, and for $\ell = L-1, \dots, 1$,

$$\mathbf{L}^{(\ell)}[i] = \mathbf{L}^{(\ell+1)}[i] (\Phi^{(\ell+1)} \mathbf{W}^{(\ell+1)}[i]). \quad (39)$$

With these definitions, for $\ell \in \{1, \dots, L\}$, the SIM output response vector $\mathbf{f}[i]$ in (12) can be represented as:

$$\mathbf{f}[i] = \mathbf{L}^{(\ell)}[i] (\Phi^{(\ell)} \mathbf{r}^{(\ell)}[i]). \quad (40)$$

B. Per-element gradient derivation

For a single subcarrier i and a given angular batch (we omit the batch index for clarity), define the residual vector

$$\mathbf{r}[i] = \mathbf{b}[i] - \mathbf{q}[i]. \quad (41)$$

The per-subcarrier contribution to the loss is $J[i] = \mathbf{r}[i]^H \mathbf{r}[i]$. By chain rule,

$$\frac{\partial J[i]}{\partial \phi_n^{(\ell)}} = 2 \Re \left\{ \left(\frac{\partial \mathbf{b}[i]}{\partial \phi_n^{(\ell)}} \right)^H \mathbf{r}[i] \right\}. \quad (42)$$

From (40) only the n -th diagonal element of $\Phi^{(\ell)}$ affects $\phi_n^{(\ell)}$, hence:

$$\frac{\partial \mathbf{b}[i]}{\partial \phi_n^{(\ell)}} = j \mathbf{A}[i]^T \mathbf{L}^{(\ell)}[i] \mathbf{e}_n e^{j\phi_n^{(\ell)}} r_n^{(\ell)}[i], \quad (43)$$

where \mathbf{e}_n is the n -th column of \mathbf{I}_N and $r_n^{(\ell)}[i]$ is the n -th entry of $\mathbf{r}^{(\ell)}[i]$. The backprojected vector $\mathbf{u}^{(\ell)}[i] \in \mathbb{C}^N$ for layer ℓ is defined as:

$$\mathbf{u}^{(\ell)}[i] = \mathbf{L}^{(\ell)}[i]^H \mathbf{A}[i]^* \mathbf{r}[i] \in \mathbb{C}^N, \quad (44)$$

and denote its n -th entry by $u_n^{(\ell)}[i]$. Substituting this into (43) and simplifying:

$$\begin{aligned} \frac{\partial J[i]}{\partial \phi_n^{(\ell)}} &= 2 \Re \left\{ -j e^{-j\phi_n^{(\ell)}} r_{i,n}^{(\ell)*} u_{i,n}^{(\ell)} \right\} \\ &= 2 \Im \left\{ e^{-j\phi_n^{(\ell)}} r_{i,n}^{(\ell)*} u_{i,n}^{(\ell)} \right\}. \end{aligned} \quad (45)$$

By stacking the gradients across $n = 1, \dots, N$, the gradient vector $\mathbf{g}^{(\ell)}[i] \in \mathbb{R}^N$ for layer ℓ can be represented as:

$$\mathbf{g}^{(\ell)}[i] = \nabla_{\Phi^{(\ell)}} J[i] = 2 \Im \left\{ \Phi^{(\ell)*} (\mathbf{r}^{(\ell)*}[i] \odot \mathbf{u}^{(\ell)}[i]) \right\}. \quad (46)$$

C. Mini-batch gradient and update rule

When using a mini-batch of N_g angular samples, the average batch loss over subcarriers can be defined as:

$$\mathcal{L}_{\text{batch}} = \frac{1}{I} \sum_{i=1}^I J[i], \quad (47)$$

whose gradient can be obtained as:

$$\nabla_{\Phi^{(\ell)}} \mathcal{L}_{\text{batch}} = \frac{1}{I} \sum_{i=1}^I \nabla_{\Phi^{(\ell)}} J[i]. \quad (48)$$

We use the Adam optimizer to update the SIM phase coefficients whose details are provided in Algorithm 3.

Algorithm 3 SIM Coefficients Optimization

- 1: **Inputs:** Initial SIM phase coefficients $\{\Phi^{(\ell)}\}$, transmission matrices $\{\mathbf{W}^{(\ell)}[i], \mathbf{w}[i]\}$, hyperparameters: learning rate η , Adam parameters $(\beta_1, \beta_2, \varepsilon)$, batch size N_g , number of batches per epoch N_b , number of epochs N_e .
 - 2: $t \leftarrow 0$, $\mathbf{m}^{(\ell)} \leftarrow 0$, $\mathbf{v}^{(\ell)} \leftarrow 0$ for $\ell = 1 : L$.
 - 3: **for** each epoch **do**
 - 4: **for** each mini-batch **do**
 - 5: Sample N_g angular grid points for this batch and form $\mathbf{A}[i]$ on the batch and obtain $\mathbf{q}[i] = \mathbf{A}[i]^T \mathbf{f}[i]$.
 - 6: **for** each subcarrier $i = 1, \dots, I$ **do**
 - 7: Compute right recursion $\mathbf{r}^{(\ell)}[i]$ for $\ell = 1 : L$
 - 8: Compute left matrices $\mathbf{L}^{(\ell)}[i]$ for $\ell = L : 1$
 - 9: Compute $\mathbf{f}[i]$ and $\mathbf{b}[i] = \mathbf{A}[i]^T \mathbf{f}[i]$.
 - 10: Compute residual $\mathbf{r}[i] = \mathbf{b}[i] - \mathbf{q}[i]$.
 - 11: Compute $\mathbf{u}^{(\ell)}[i] = \mathbf{L}^{(\ell)H}[i] \mathbf{A}[i]^* \mathbf{r}[i]$.
 - 12: Obtain the gradient vectors $\mathbf{g}^{(\ell)}[i]$ using (46) for $\ell = 1 : L$.
 - 13: **end for**
 - 14: Compute the average batch gradient $\bar{\mathbf{g}}^{(\ell)} = \frac{1}{IN_g} \sum_{i=1}^I \mathbf{g}^{(\ell)}[i]$.
 - 15: **Adam moment updates:**
 $t \leftarrow t + 1$,
 $\mathbf{m}^{(\ell)} \leftarrow \beta_1 \mathbf{m}^{(\ell)} + (1 - \beta_1) \bar{\mathbf{g}}^{(\ell)}$,
 $\mathbf{v}^{(\ell)} \leftarrow \beta_2 \mathbf{v}^{(\ell)} + (1 - \beta_2) (\bar{\mathbf{g}}^{(\ell)} \odot \bar{\mathbf{g}}^{(\ell)})$,
 $\hat{\mathbf{m}}^{(\ell)} = \frac{\mathbf{m}^{(\ell)}}{1 - \beta_1^t}$, $\hat{\mathbf{v}}^{(\ell)} = \frac{\mathbf{v}^{(\ell)}}{1 - \beta_2^t}$.
 - 16: **Phase coefficients update:**
 $\Phi^{(\ell)} \leftarrow \text{wrap} \left(\Phi^{(\ell)} - \eta \frac{\hat{\mathbf{m}}^{(\ell)}}{\sqrt{\hat{\mathbf{v}}^{(\ell)} + \varepsilon}} \right)$, where $\text{wrap}(\cdot)$ projects angles into $(-\pi, \pi]$.
 - 17: **end for**
 - 18: **end for**
-

VI. COMPLEXITY ANALYSIS

A. Complexity of Algorithms 1 and 2

The dominant computational burden in Algorithm 1 is the repeated computation of the principal eigenvector of the shifted matrix $\mathbf{A} - \mu \mathbf{R}$ during the bisection/bracketing phase. Let M_1 denote the number of bisection iterations needed to reach the tolerance ξ_{tol} and by $T_{\text{eig}}(N)$ the cost of a single principal-eigenpair computation, the per-subcarrier complexity is $O(M_1 T_{\text{eig}}(N))$. Thus, for I subcarriers the overall complexity scales as $O(I M_1 T_{\text{eig}}(N))$. Note that a full eigenvalue decomposition incurs complexity $T_{\text{eig}} = O(N^3)$. However, since only the principal eigenvector is required, much more efficient iterative methods (e.g., Lanczos) can be employed using a few matrix-vector products per iteration (roughly $O(N^2)$ per iteration for dense matrices) with fast convergence [41, Chap. 10]. Regarding the outer optimization, since $\mathbf{J}_B \in \mathbb{R}^{5 \times 5}$, the closed form solution (34) of $\{\mathbf{d}_j\}_{j=1}^3$ has the complexity $O(1)$. Hence, the complexity of Algorithm 2, can be obtained as $O(I M_2 M_1 T_{\text{eig}}(N))$ where M_2 is the average number of the alternating iterations until convergence. In Sec. VII-B, Monte-Carlo simulations are conducted to

demonstrate the convergence behavior of these algorithms.

B. Complexity of Algorithm 3

The dominant cost inside each mini-batch arises from constructing the backward left matrices and performing dense matrix-matrix and matrix-vector products for each subcarrier. Conservatively, the per-mini-batch complexity scales as $O(I(LN^3 + N_g N + LN^2))$, so that the total training complexity is $O(N_e N_b I(LN^3 + N_g N + LN^2))$, and in the large- N regime is dominated by $O(N_e N_b I L N^3)$. It is noteworthy that, despite the obtained asymptotic arithmetic cost, parallelizing across subcarriers and batches and using optimized GPU kernels, substantially reduces this cost.

Remark 1. While we assume quasi-static channels in this paper, Algorithm 3 can be adapted to real-time scenarios by initializing with the previous optimized phase coefficients and performing limited online fine-tuning (small batches and learning rates), or by using precomputed phase-codebooks [9], [40], [42]. The details are left for future work.

VII. SIMULATIONS

In this section, we evaluate the performance of the proposed methods for SIM-assisted mmWave systems through extensive numerical simulations.

A. Simulation Setup

The SIM layers are assumed to be equipped with a UPA with the same number of rows and columns $N^h = N^v$. For the SU's state parameter vector's prior p_γ , we assume a uniform distribution inside the cuboid specified by $50 \leq x \leq 70$, $-10 \leq y \leq 10$, and $0 \leq z \leq 5$. The number of $M_p = 20000$ points are generated based on the prior p_γ to estimate the expectation \mathbb{E}_γ in (19). The positions of the components of the considered system as well as the uncertainty region for the SU are shown in Fig. 2, the default system and algorithmic parameters are presented in Table I, and Table II, respectively. In all simulations except Sec. VII-F, we use $N_{pu} = 2$ PUs (i.e., PU 1 and PU 2 depicted in Fig. 2). For the SIM's geometry parameters including the area of each meta-atom and inter-layer distance, trial and error and also inspiration from the existing literature (e.g., [10], [35]) were used to obtain suitable parameters which are shown in Table I. Moreover, the number of $Q_{su,s} = Q_{pu,s} = Q_{su,pb} = Q_{pu,pb} = 50$ single-point scatterers are randomly generated in the environment to model MPCs for the geometric channels in (5).

It is noteworthy that according to (2), due to different amplitudes in transmission matrices $\mathbf{W}^{(\ell)}[i]$ between layers, the gain of the end-to-end SIM response in (3) or (12), may vary for different numbers of SIM meta-atoms N and the number of layers L . Thus, for a fair comparison in different simulations, we define the total transmitted power from the SWS i.e., the total radiated power from the SIM's output layer as:

$$P_{sws} = \frac{IP_{sb}}{\sum_{i=1}^I \|\mathbf{f}[i]\|^2}, \quad (49)$$

which is set to $P_{sws} = 30$ dBm as a default value, and the PB power is fixed at $P_{pb} = 30$ dBm by default. It is noteworthy that by interpreting the SB omni-antenna and SIM as an adaptive antenna, P_{sws} corresponds to the the product of

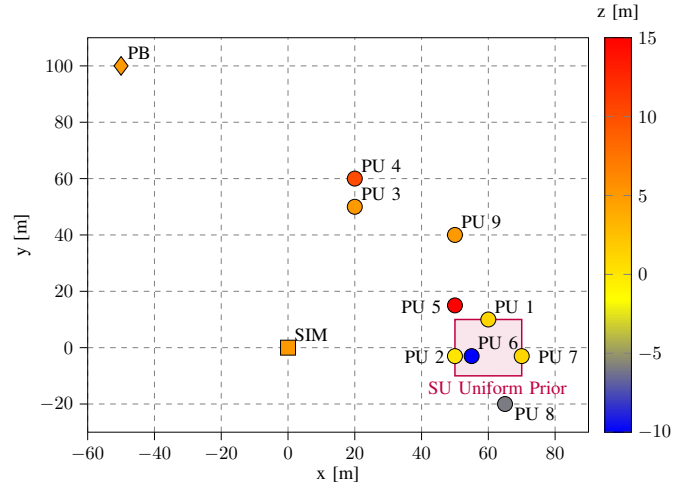


Fig. 2: Positions of the SIM, PB, PUs, and the SU uncertainty region considered in the simulations based on the selected uniform prior. The colorbar shows the corresponding z value coordinates.

conducted power and antenna efficiency. Under these power levels, we choose the QoS parameter $\kappa = 98\%$ in (26b). Note that some parameters in this subsection may differ across different simulation scenarios.

TABLE I: System parameters.

Default System Parameters and Symbol	Value
Light speed c	3×10^8 m/s
Carrier frequency f_c and wavelength $\lambda_c = c/f_c$	30 GHz, 1 cm
Noise PSD N_0	-173.855 dBm
Underlay bandwidth B	50 MHz
Underlay subcarrier spacing Δf	1 MHz
SWS transmit power P_{sws}	30 dBm
PB transmit power P_{pb}	30 dBm
QoS parameter κ in (26b)	98%
Frequency of the i -th subcarrier f_i	$f_c - (i-1)\Delta f$
SB position \mathbf{p}_{sb}	$[0, 0, 5]^T$
PB position \mathbf{p}_{pb}	$[-50, 100, 5]^T$
Number of SIM layers L	4
Inter-layer distance in the SIM d_s	$3\lambda_c/2$
Distance between two adjacent meta-atoms d	$\lambda_c/2$
Area of each meta-atom A_s	$\lambda_c/2$
SIM per-layer number of rows and columns N^h, N^v	6, 6
Number of generated points M_p to estimate \mathbb{E}_γ	20000
Upper bounds $\delta[i]$ in (27c)	1

TABLE II: Algorithmic parameters.

Parameter	Value
Parameter ξ_{tol} in Algorithm 1	10^{-20}
Parameters $\varepsilon_{tol}, \tau_{tol}$ in Algorithm 2	$10^{-12}, 10^{-12}$
Number of epochs N_e	200
Number of batches per epoch	50
Batch size N_d	512
Learning rate η	0.001
First moment exponential decay rate β_1	0.9
Second moment exponential decay rate β_2	0.999
Numerical stability constant ε	10^{-8}

B. Convergence Analysis of Algorithms 1 and 2

To assess the performance of the proposed AO-based Algorithm 2, Fig. 3 illustrates the BCRB versus number of iterations for SIM layer sizes $N^h = N^v \in \{5, 6, 7, 8\}$. The results are averaged over 200 Monte-Carlo trials. According to the results, the algorithm converges rapidly, within approximately 4 iterations.

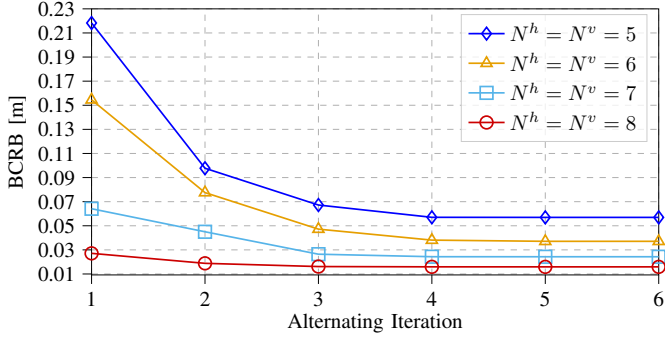


Fig. 3: performance of the AO based Algorithm 2.

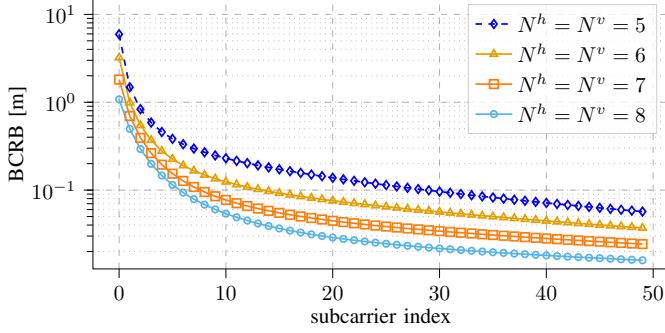


Fig. 4: BCRB values after optimizing $\mathbf{f}[i]$ for $i = 1, \dots, I$.

Remark 2. In the simulations that follow, the optimized end-to-end SIM response vectors $\{\hat{\mathbf{f}}[i]\}_{i=1}^I$ produced by Algorithm 2 are hereafter referred to as the optimal estimates of $\{\mathbf{f}[i]\}_{i=1}^I$. As detailed in Sec. V, the SIM coefficients are trained to reproduce the beampatterns corresponding to these optimal vectors, i.e., to match the target beampatterns as closely as possible.

To evaluate the performance of Algorithm 1 we initialize the vectors $\{\mathbf{f}[i]\}_{i=1}^I$ randomly, and fix the vectors $\{\mathbf{d}_j\}_{j=1}^3$ using the optimal values in the last iteration of Algorithm 2. Then, we execute Algorithm 1 to optimize $\{\mathbf{f}[i]\}_{i=1}^I$. Fig. 4 shows the BCRB after sequentially optimizing each $\mathbf{f}[i]$, $i = 1, \dots, I$, with Algorithm 1 for SIM layer sizes $N^h = N^v \in \{5, 6, 7, 8\}$. The curves evidently decrease with the subcarrier index, which demonstrates the convergence and effectiveness of the proposed algorithm. As stated in Prop. 2, since each subcarrier can be optimized independently, the subcarrier update order does not affect the final BCRB i.e., different ordering choices converge to the same solution.

Fig. 5 shows the relative objective $g(\mu)/\epsilon = \mathbf{v}(\mu)^H \mathbf{R} \mathbf{v}(\mu) / \epsilon$ (i.e., relative interference energy) produced by the bisection subroutine in Algorithm 1, plotted against the iteration index. Individual per-subcarrier objective values are plotted together with their mean. The results indicate that the proposed bisection routine converges to the optimal value 1 within approximately 10 iterations for every subcarrier, demonstrating the efficiency and robustness of the proposed method to satisfy the interference constraint (26b) (or equivalent constraint (27b)) for inner optimization of (29).

C. Training SIM and Convergence Analysis

Algorithm 3 is employed to train the SIM phase coefficients. Training is performed for $N_e = 200$ epochs with

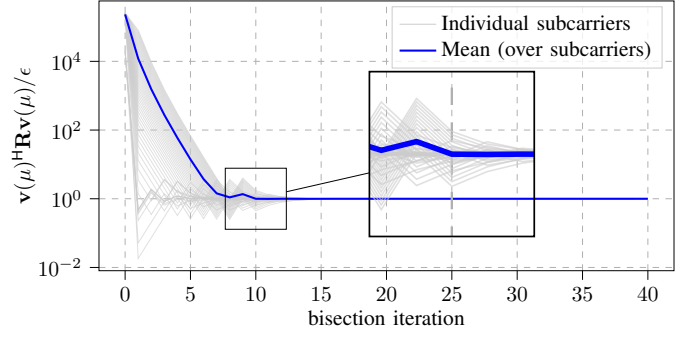
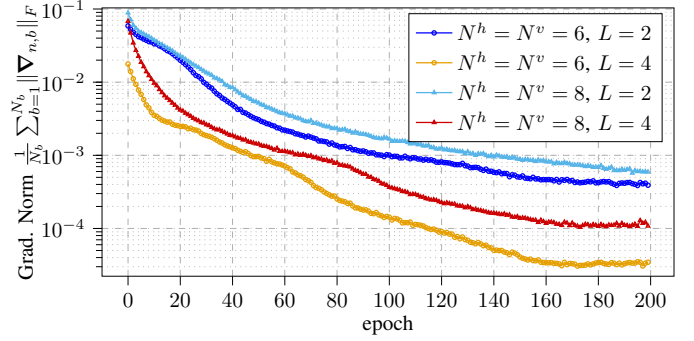
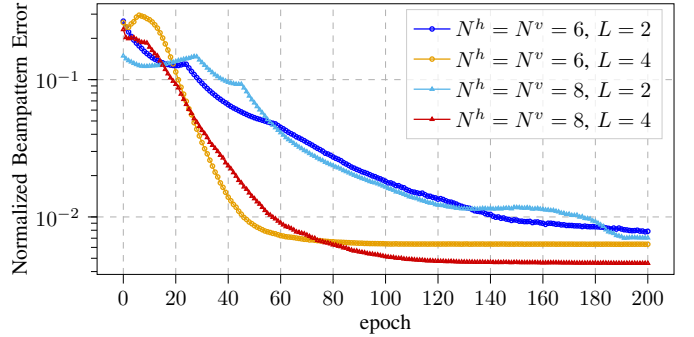


Fig. 5: Relative interference energy per bisection iteration for different subcarriers. The average curve over all subcarriers is also shown.



(a) Average gradient norms versus epoch to assess convergence behavior.



(b) Normalized beampattern error during training versus epoch.
Fig. 6: Convergence analysis of the proposed Algorithm 3.

$N_b = 50$ batches per epoch, each batch containing $N_d = 512$ samples. Detailed training parameters are given in Table II. Let $\nabla_{e,b} \in \mathbb{C}^{L \times N}$ denote the gradient computed at epoch e and batch b , and define the epoch-averaged gradient norm $\bar{g}_e = \frac{1}{N_b} \sum_{b=1}^{N_b} \|\nabla_{e,b}\|_F$. Fig. 6a plots \bar{g}_e versus epoch e for $N^h = N^v \in \{6, 8\}$ and $L \in \{2, 4\}$, which demonstrate convergence of the training. The corresponding normalized beampattern difference between the SIM and the optimal beampattern are shown in Fig. 6b, further confirming convergence of the training process.

D. Beampattern Analysis

Fig. 7 presents examples of the normalized 2D beampatterns for the first subcarrier comparing the analytically obtained optimal response and the trained SIM for layer counts $L \in \{1, 2, 3, 4\}$. Note that $L = 1$ corresponds to a conventional RIS operating in diffraction mode. The 2D-AODs of the PUs are indicated in each subplot. For $L \in \{1, 2\}$ the trained SIM shows a large mismatch to the optimal beampattern and does not sufficiently attenuate power at the PUs. By contrast, when

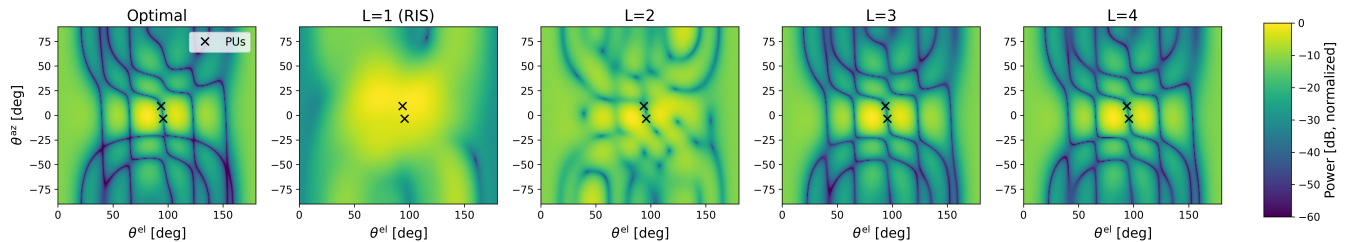
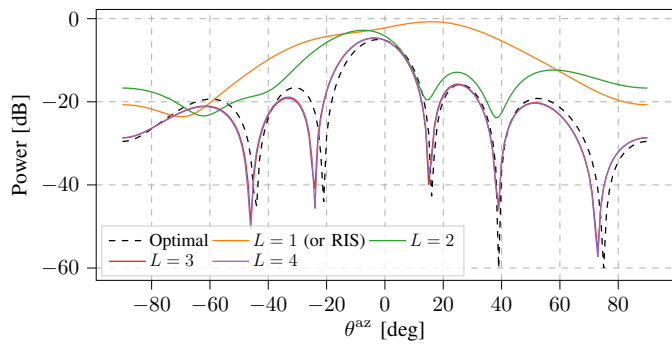
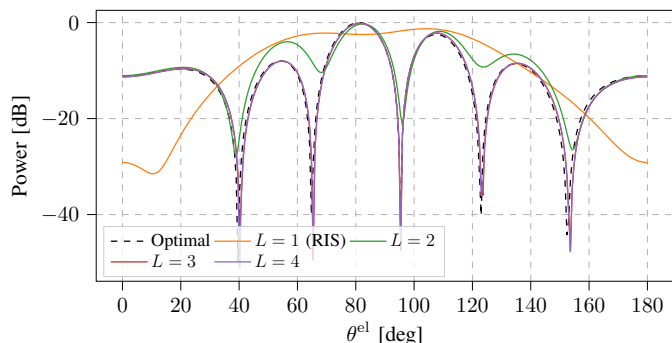


Fig. 7: 2D-Beampatterns of the trained SIMs with fixed $N^h = N^v = 6$ and different number of layers $L \in \{1, 2, 3, 4\}$.



(a) 1D beampattern comparison for fixed $\theta^{el} = 90^\circ$



(b) 1D beampattern comparison for fixed $\theta^{az} = 0^\circ$

Fig. 8: Two 1D cuts of the 2D beampatterns to better compare the performance of the trained SIM for different number of layers.

$L \in \{3, 4\}$ the trained SIM closely reproduces the optimal beampattern and the PUs 2D-AODs lie at the beampattern nulls. To facilitate comparison, in Fig. 8, we plot two 1D cuts of the 2D beampatterns from Fig. 7 taken at fixed angles $\theta^{el} = 90^\circ$ and $\theta^{az} = 0^\circ$. The plots confirm that the SIMs with $L \in \{3, 4\}$ closely reproduce the optimal beampattern.

E. Localization and Spectral Efficiency Performance

In this subsection, we evaluate the localization and SE performance of the proposed methods. Fig. 9 shows the BCRB obtained with trained SIMs having $L = 4$ layers versus P_{sws} (defined in (49)). It is observed that the learned responses closely track the corresponding optimal values, demonstrating the performance of Algorithm 3. To quantify the effect of the number of layers, Fig. 10 compares the BCRB for trained SIMs with $N^h = N^v \in \{6, 8\}$ and $L \in \{1, 2, 3, 4\}$ at a fixed power $P_{\text{sws}} = 20$ dBm, showing that localization performance improves with L and essentially converges to the optimal end-to-end response by $L = 4$. Hence, for the considered system, a four-layer SIM is sufficient to achieve optimal localization.

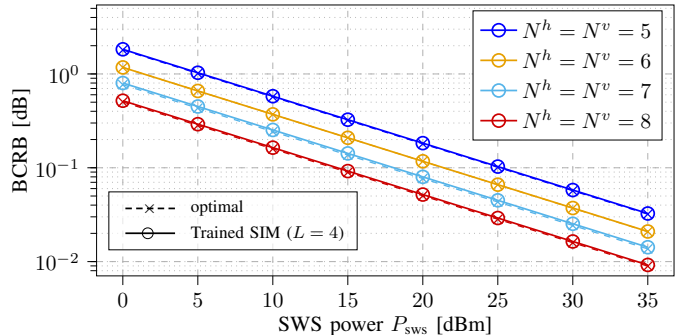


Fig. 9: BCRB values versus P_{sws} using trained SIMs with $L = 4$ layers.

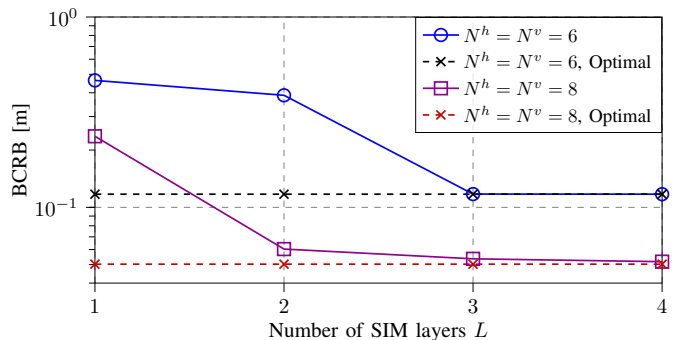


Fig. 10: BCRB of the trained SIMs versus L at $P_{\text{sws}} = 20$ dBm.

The average SE, defined as $\frac{1}{I} \sum_{i=1}^I \log(1 + \text{SINR}[i])$ (with $\text{SINR}[i]$ given in (22)), is plotted in Fig. 11 versus P_{sws} for trained SIMs with $N^h = N^v = 6$ and $L \in \{1, 2, 3, 4\}$ at a fixed PB transmit power $P_{\text{pb}} = 30$ dBm where the optimal SE curve is also shown as a baseline. Evidently, the trained SIM with $L = 4$ closely achieves the optimal performance.

Likewise, the corresponding SE are shown in terms of PB power P_{pb} in Fig. 12. The SIM with $L = 4$ achieves near-optimal SE across the considered power range, and SIMs with $L \geq 2$ substantially outperform the single-layer RIS. These results demonstrate that multi-layer SIMs are capable of learning and realizing the sophisticated multi-functional beampatterns required to jointly support SU localization and PU interference management.

F. Robustness Under Different Number of PUs

In this subsection we evaluate the proposed methods as the number of active PUs varies. We consider a set of nine candidate PUs whose locations are shown in Fig. 2. For each $N_{\text{pu}} \in \{1, 3, 5, 7, 9\}$ the first N_{pu} positions are treated as active and the SIM is trained for that scenario. Fig. 13 presents the resulting 2D beampatterns with the corresponding 2D-AODs of the active PUs indicated. In every case the trained SIM places

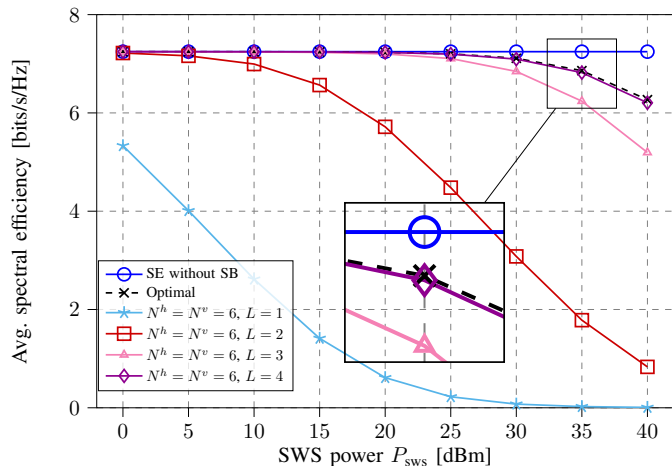


Fig. 11: Average SE versus P_{sws} at a fixed $P_{\text{pb}} = 30$ dBm.

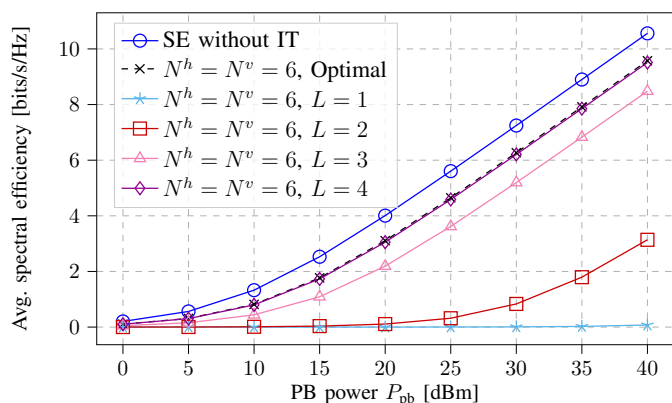


Fig. 12: Average SE versus P_{pb} at a fixed $P_{\text{sws}} = 40$ dBm.

deep nulls at the active-PU directions to satisfy the interference constraint, yielding distinct beam patterns as N_{pu} changes. The corresponding BCRB values are illustrated in Fig. 14. As expected, increasing N_{pu} generally increases the BCRB (i.e., degrades localization accuracy) because more stringent PU protection reduces the degrees of freedom available for localization. The magnitude of this degradation, however, is geometry-dependent: when active PUs lie close to or inside the SU uncertainty region (e.g., PUs 1, 2, 6, and 7 in Fig. 2), the performance penalty is larger.

VIII. CONCLUSION

This paper investigated a multi-functional SIM-assisted CR-ISAC downlink framework. We integrated the SB with a multi-layer SIM and adopted the BCRB as the localization performance metric. We then formulated a BCRB-minimization problem subject to an average PU SE constraint that limits performance degradation to at most a few percent. To design the SIM coefficients we cast the problem as a constrained nonconvex problem, reformulated it into a tractable max-min form and developed an efficient AO-based algorithm (inner minimization via bisection and an outer step in closed form). Building on the SIM/DNN analogy, we also derived analytical gradients for backpropagation and proposed an Adam-based, mini-batch learning scheme that uses a beam pattern-matching loss to realize the optimal end-to-end response. Extensive numerical results confirm fast convergence of the proposed algorithms and demonstrate that multi-layer SIMs

(in particular $L = 4$) can achieve near-optimal beam patterns and substantially outperform single-layer RIS designs for joint localization and interference management. Future work will extend the present study to real-time scenarios and also account for practical implementation aspects, including hardware impairments, and develop maximum-likelihood estimators.

APPENDIX A PROOF OF PROP. 1

The semidefinite relaxation (SDR) version of the optimization problem (27) can be obtained as follows:

$$\min_{\{\mathbf{F}[i]\}_{i=1}^I} \text{BCRB}(\{\mathbf{F}[i]\}_{i=1}^I) \quad (50a)$$

$$\text{s.t. } \epsilon[i] \geq \mathbf{R}_{\text{pu}} \bullet \mathbf{F}[i], \quad (50b)$$

$$\text{tr}(\mathbf{F}[i]) \leq \delta[i], \quad i = 1, \dots, I, \quad (50c)$$

where we have dropped the rank-1 constraints $\mathbf{F}[i] = \mathbf{f}[i]\mathbf{f}[i]^H$ to make the problem convex. Note that:

$$\text{BCRB} = \text{tr}([\mathbf{J}_B^{-1}]_{1:3, 1:3}) = \sum_{j=1}^3 \mathbf{e}_j^T \mathbf{J}_B^{-1} \mathbf{e}_j. \quad (51)$$

Next, we write the epigraph form of (50) as follows:

$$\min_{\{\mathbf{F}[i]\}_{i=1}^I, \{t_j\}_{j=1}^3} \sum_{j=1}^3 t_j \quad (52a)$$

$$\text{s.t. } \begin{bmatrix} \mathbf{J}_B(\{\mathbf{F}[i]\}_{i=1}^I) & \mathbf{e}_j \\ \mathbf{e}_j^T & t_j \end{bmatrix} \succeq 0, \quad (52b)$$

$$j = 1, 2, 3,$$

$$(50b), (50c)$$

where we have used the Schur complement technique [40], [43] to obtain the linear matrix inequality (LMI) (52b) which is equivalent to $t_j \geq \mathbf{e}_j^T \mathbf{J}_B^{-1} \mathbf{e}_j$. The Lagrangian of the problem with respect to (52b) is defined as:

$$\mathcal{L} = \sum_{j=1}^3 t_j - \sum_{j=1}^3 \mathbf{D}_j \bullet \mathbf{B}_j \quad (53)$$

where \mathbf{B}_j is the matrix in (52b), and $\mathbf{D}_j \succeq 0$ denotes the dual variables with respect to the LMI (52b). By partitioning \mathbf{D}_j as

$$\mathbf{D}_j = \begin{bmatrix} \bar{\mathbf{D}}_j & -\mathbf{d}_j \\ -\mathbf{d}_j^T & d_j \end{bmatrix},$$

the Lagrangian (53) can be rewritten as:

$$\mathcal{L} = \sum_{j=1}^3 t_j(1 - d_j) - \sum_{j=1}^3 \bar{\mathbf{D}}_j \bullet \mathbf{J}_B + 2 \sum_{j=1}^3 \mathbf{e}_j^T \mathbf{d}_j. \quad (54)$$

The dual function is found by minimizing the Lagrangian over the primal variables, $\{\mathbf{F}[i]\}_{i=1}^I$ and $\{t_j\}_{j=1}^3$. By setting the derivative with respect to t_j to zero, we obtain $d_j = 1$, because otherwise the minimum is unbounded. Applying the Schur complement to the constraint $\mathbf{D}_j \succeq 0$, we obtain the equivalent constraint $\bar{\mathbf{D}}_j \succeq \mathbf{d}_j \mathbf{d}_j^T$. Thus, the dual problem is obtained as:

$$\max_{\{\bar{\mathbf{D}}_j\}_{j=1}^3} \min_{\{\mathbf{F}[i]\}_{i=1}^I} - \sum_{u=1}^3 \bar{\mathbf{D}}_u \bullet \mathbf{J}_B + 2 \sum_{u=1}^3 \mathbf{e}_u^T \mathbf{d}_u, \quad (55a)$$

$$\text{s.t. } (50b), (50c)$$

Hence, since strong duality holds, the duality gap is zero, meaning the optimal values of the primal and dual problems

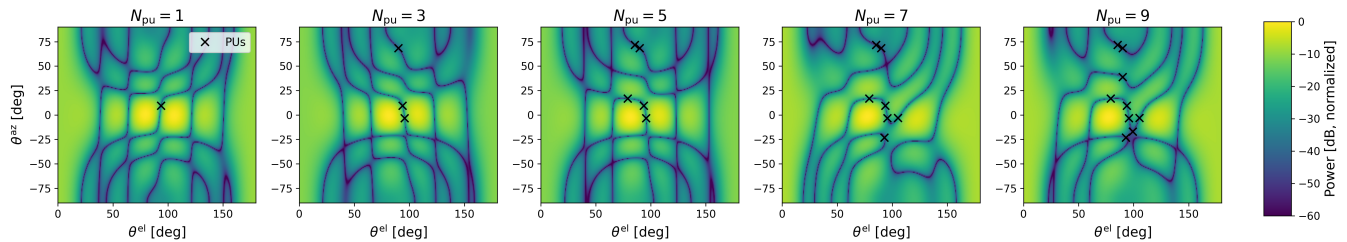


Fig. 13: 2D-Beampatterns of the trained SIMs (with $L = 4$ layers and $N^h = N^v = 6$) for different number of active PUs.

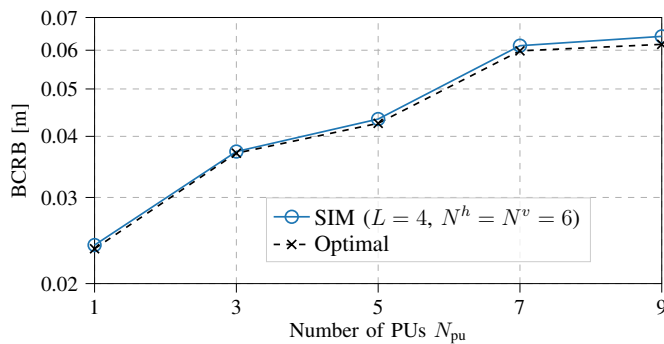


Fig. 14: BCRB versus number of PUs at $P_{\text{sws}} = 30$ dBm.

are equal. This allows us to interchange min and max in (55) and first find the optimal $\bar{\mathbf{D}}_j$ [44]. Since $\bar{\mathbf{D}}_j \succeq \mathbf{d}_j \mathbf{d}_j^T$ and $\mathbf{J}_B \succeq 0$, we have $\bar{\mathbf{D}}_j \bullet \mathbf{J}_B \geq \mathbf{d}_j \mathbf{d}_j^T \bullet \mathbf{J}_B$, from which we conclude that at the optimum we have $\bar{\mathbf{D}}_j = \mathbf{d}_j \mathbf{d}_j^T$. Moreover, after substituting this result back into (55), we obtain (29). By substituting (19) in (17), and then (17) in (29a), (29) can be represented as (30). By [45, Prop. 3.5], for any fixed vectors $\{\mathbf{d}_j\}_{j=1}^3$ problem (30) admits rank-one optimal solutions of the form $\hat{\mathbf{F}}[i] = \hat{\mathbf{f}}[i] \hat{\mathbf{f}}[i]^H$, which completes the proof.

APPENDIX B PROOF OF PROP. 2

We rewrite the inner optimization problem as follows:

$$\max_{\mathbf{f} \in \mathbb{C}^N} \mathbf{f}^H \mathbf{A} \mathbf{f} \quad \text{s.t.} \quad \mathbf{f}^H \mathbf{R} \mathbf{f} \leq \epsilon, \quad \|\mathbf{f}\|^2 \leq \delta.$$

We form the Lagrangian with multipliers $\mu \geq 0$ (for the PU constraint) and $\lambda \geq 0$ (for the power constraint):

$$\mathcal{L}(\mathbf{f}, \mu, \lambda) = \mathbf{f}^H \mathbf{A} \mathbf{f} - \mu(\mathbf{f}^H \mathbf{R} \mathbf{f} - \epsilon) - \lambda(\mathbf{f}^H \mathbf{f} - \delta). \quad (56)$$

After setting the derivative with respect to \mathbf{f} to zero we obtain:

$$(\mathbf{A} - \mu \mathbf{R} - \lambda \mathbf{I}) \hat{\mathbf{f}} = \mathbf{0}. \quad (57)$$

From complementary slackness and feasibility:

$$\mu(\hat{\mathbf{f}}^H \mathbf{R} \hat{\mathbf{f}} - \epsilon) = 0, \quad \lambda(\hat{\mathbf{f}}^H \hat{\mathbf{f}} - \delta) = 0, \quad (58)$$

Next, We consider three cases:

A. *Case 1:* $\lambda_{\max}(\mathbf{A}) \leq 0$

In this case it is easy to observe that $\hat{\mathbf{f}} = \mathbf{0}$.

B. *Case 2:* $\lambda_{\max}(\mathbf{A}) \geq 0$ with feasible principal eigenvector

Let \mathbf{u} be a principal unit eigenvector of \mathbf{A} associated to $\lambda_{\max}(\mathbf{A})$. If $\mathbf{u}^H \mathbf{R} \mathbf{u} \leq \frac{\epsilon}{\delta}$, then $\hat{\mathbf{f}} = \sqrt{\delta} \mathbf{u}$ is feasible and attains the objective value $\delta \lambda_{\max}(\mathbf{A})$, and the PU multiplier μ is zero.

C. *Case 3:* $\lambda_{\max}(\mathbf{A}) \geq 0$ with infeasible principal eigenvector

If the inequality in the previous case is violated i.e., $\mathbf{u}^H \mathbf{R} \mathbf{u} > \frac{\epsilon}{\delta}$, the PU interference constraint must be active

at optimum (i.e. $\mu > 0$) [44]. Since $\hat{\mathbf{f}} \neq \mathbf{0}$ then (57) implies $\hat{\mathbf{f}}$ lies in the nullspace of the Hermitian matrix $\mathbf{A} - \mu \mathbf{R} - \lambda \mathbf{I}$, or equivalently $\hat{\mathbf{f}}$ is an eigenvector of $\mathbf{A} - \mu \mathbf{R}$ with eigenvalue λ . Thus, if we define $\mathbf{v} = \hat{\mathbf{f}}/\sqrt{\delta}$, we conclude that the optimal unit-norm direction \mathbf{v} is the principal eigenvector of the Hermitian matrix: $\mathbf{M}(\mu) \triangleq \mathbf{A} - \mu \mathbf{R}$, and the equality constraint to enforce is:

$$\mathbf{v}(\mu)^H \mathbf{R} \mathbf{v}(\mu) = \frac{\epsilon}{\delta}. \quad (59)$$

Thus the problem reduces to finding a scalar $\mu \geq 0$ such that the principal eigenvector $\mathbf{v}(\mu)$ of $\mathbf{M}(\mu)$ satisfies (59). Once μ is found, the optimizer is $\hat{\mathbf{f}} = \sqrt{\delta} \mathbf{v}(\mu)$.

We propose to use bisection root-finding algorithm to the scalar function $h(\mu) = g(\mu) - \epsilon/\delta$. Under the usual non-degeneracy assumption that the principal eigenvalue of $\mathbf{M}(\mu)$ is simple, $\mathbf{v}(\mu)$ (and hence $g(\mu)$) depends continuously on μ , so $h(\mu)$ is continuous. We therefore first obtain a bracket $[\mu_\ell, \mu_u]$ (using $\mu_\ell = 0$ and $\mu_u = 1$ as initial values) by doubling $\mu_u \leftarrow 2\mu_u$ until $h(\mu_u) \leq 0$ (i.e. $g(\mu_u) \leq \epsilon/\delta$), which ensures $h(\mu_\ell) \geq 0$ and $h(\mu_u) \leq 0$. Bisection method then iterates by evaluating $g(\mu)$ at $\mu = \frac{\mu_\ell + \mu_u}{2}$, and replaces the left or right endpoint according to the sign of $h(\mu)$, until $|h(\mu)| < \xi_{\text{tol}}$. The details are also presented in Algorithm 1.

APPENDIX C PROOF OF PROP. 3

The objective in (33) is the sum of three decoupled quadratic functions $\ell_j(\mathbf{d}_j) = 2\mathbf{e}_j^T \mathbf{d}_j - \mathbf{d}_j^T \mathbf{J}_B \mathbf{d}_j$. Setting the derivative to zero, we obtain the linear normal equation $2\mathbf{e}_j - 2\mathbf{J}_B \mathbf{d}_j = \mathbf{0}$ which can be rewritten as $\mathbf{J}_B \mathbf{d}_j = \mathbf{e}_j$. Since \mathbf{J}_B is positive definite, the linear system has the unique solution (34).

APPENDIX D

PROOF OF LEMMA 1

First we partition \mathbf{J}_B as

$$\mathbf{J}_B = \begin{bmatrix} \mathbf{U} & \mathbf{V} \\ \mathbf{V}^T & \mathbf{W} \end{bmatrix},$$

where $\mathbf{U} \in \mathbb{R}^{3 \times 3}$, $\mathbf{V} \in \mathbb{R}^{3 \times 2}$ and $\mathbf{W} \in \mathbb{R}^{2 \times 2}$. Since $\mathbf{J}_B \succ 0$, the block \mathbf{W} is invertible and the Schur complement of \mathbf{W} is defined as $\mathbf{S} = \mathbf{U} - \mathbf{V} \mathbf{W}^{-1} \mathbf{V}^T$. By standard block-inverse formula the top-left 3×3 block of \mathbf{J}_B^{-1} equals \mathbf{S}^{-1} ; equivalently,

$$[\mathbf{J}_B^{-1}]_{1:3,1:3} = \mathbf{S}^{-1} \rightarrow \text{tr}([\mathbf{J}_B^{-1}]_{1:3,1:3}) = \text{tr}(\mathbf{S}^{-1}). \quad (60)$$

Let the eigenvalues of \mathbf{S} be $\mu_1, \mu_2, \mu_3 > 0$. Then $\text{tr}(\mathbf{S}) = \sum_{i=1}^3 \mu_i$ and $\text{tr}(\mathbf{S}^{-1}) = \sum_{i=1}^3 \mu_i^{-1}$. By the Cauchy-Schwarz inequality:

$$\left(\sum_{i=1}^3 \mu_i \right) \left(\sum_{i=1}^3 \frac{1}{\mu_i} \right) \geq \left(\sum_{i=1}^3 1 \right)^2 = 9,$$

which gives

$$\text{tr}(\mathbf{S}^{-1}) \geq \frac{9}{\text{tr}(\mathbf{S})}. \quad (61)$$

Because $\mathbf{V}\mathbf{W}^{-1}\mathbf{V}^T \succeq 0$ we have $\mathbf{S} \preceq \mathbf{U}$ in the positive semi-definite (PSD) order, and therefore

$$\text{tr}(\mathbf{S}) \leq \text{tr}(\mathbf{U}). \quad (62)$$

Combining (60), (61) and (62) yields

$$\text{tr}([\mathbf{J}_B^{-1}]_{1:3,1:3}) = \text{tr}(\mathbf{S}^{-1}) \geq \frac{9}{\text{tr}(\mathbf{S})} \geq \frac{9}{\text{tr}(\mathbf{U})},$$

which proves the claim.

REFERENCES

- [1] P. Yang *et al.*, “6G wireless communications: Vision and potential techniques,” *IEEE Network*, vol. 33, no. 4, pp. 70–75, 2019.
- [2] H. Tataria *et al.*, “6G wireless systems: Vision, requirements, challenges, insights, and opportunities,” *Proceedings of the IEEE*, vol. 109, no. 7, pp. 1166–1199, 2021.
- [3] J. Yuan *et al.*, “A two-timescale resource allocation scheme for RIS-aided cognitive radio systems,” *IEEE Transactions on Cognitive Communications and Networking*, pp. 1–1, 2025.
- [4] Y.-C. Liang *et al.*, “Cognitive radio networking and communications: an overview,” *IEEE Transactions on Vehicular Technology*, vol. 60, no. 7, pp. 3386–3407, 2011.
- [5] Y. Xu *et al.*, “RIS-enhanced cognitive integrated sensing and communication: Joint beamforming and spectrum sensing,” *IEEE Journal on Selected Areas in Communications*, vol. 43, no. 3, pp. 795–810, 2025.
- [6] A. F. Molisch, *Wireless communications: from fundamentals to beyond 5G*. John Wiley & Sons, 2022.
- [7] B. Wang *et al.*, “Advances in cognitive radio networks: A survey,” *IEEE Journal of Selected Topics in Signal Processing*, vol. 5, no. 1, pp. 5–23, 2011.
- [8] M. El Tanab *et al.*, “Resource allocation for underlay cognitive radio networks: A survey,” *IEEE Communications Surveys & Tutorials*, vol. 19, no. 2, pp. 1249–1276, 2017.
- [9] A. Fadakar *et al.*, “Mutual coupling-aware localization for RIS-assisted ISAC systems,” *IEEE Transactions on Cognitive Communications and Networking*, vol. 11, no. 5, pp. 2938–2954, 2025.
- [10] J. An *et al.*, “Two-dimensional direction-of-arrival estimation using stacked intelligent metasurfaces,” *IEEE Journal on Selected Areas in Communications*, vol. 42, no. 10, pp. 2786–2802, 2024.
- [11] N. González-Prelcic *et al.*, “The integrated sensing and communication revolution for 6G: Vision, techniques, and applications,” *Proceedings of the IEEE*, vol. 112, no. 7, pp. 676–723, 2024.
- [12] J. An *et al.*, “Stacked intelligent metasurfaces for multiuser downlink beamforming in the wave domain,” *IEEE Transactions on Wireless Communications*, vol. 24, no. 7, pp. 5525–5538, 2025.
- [13] H. Niu *et al.*, “Stacked intelligent metasurfaces for integrated sensing and communications,” *IEEE Wireless Communications Letters*, vol. 13, no. 10, pp. 2807–2811, 2024.
- [14] Y. Liu *et al.*, “Reconfigurable intelligent surfaces: Principles and opportunities,” *IEEE Communications Surveys & Tutorials*, vol. 23, no. 3, pp. 1546–1577, 2021.
- [15] C. Pan *et al.*, “An overview of signal processing techniques for RIS/IRS-aided wireless systems,” *IEEE Journal of Selected Topics in Signal Processing*, vol. 16, no. 5, pp. 883–917, 2022.
- [16] A. Fascista *et al.*, “RIS-aided joint localization and synchronization with a single-antenna receiver: Beamforming design and low-complexity estimation,” *IEEE Journal of Selected Topics in Signal Processing*, vol. 16, no. 5, pp. 1141–1156, 2022.
- [17] A. Fadakar *et al.*, “Multi-RIS-assisted 3D localization and synchronization via deep learning,” *IEEE Open Journal of the Communications Society*, vol. 5, pp. 3299–3314, 2024.
- [18] —, “Near-field RIS-assisted localization under mutual coupling,” in *2025 IEEE International Conference on Communications Workshops (ICC Workshops)*, 2025, pp. 1470–1475.
- [19] J. An *et al.*, “Stacked intelligent metasurfaces for multiuser beamforming in the wave domain,” in *ICC 2023 - IEEE International Conference on Communications*, 2023, pp. 2834–2839.
- [20] —, “Stacked intelligent metasurfaces for efficient holographic MIMO communications in 6G,” *IEEE Journal on Selected Areas in Communications*, vol. 41, no. 8, pp. 2380–2396, 2023.
- [21] H. Liu *et al.*, “Multi-user MISO with stacked intelligent metasurfaces: A DRL-based sum-rate optimization approach,” *IEEE Transactions on Cognitive Communications and Networking*, pp. 1–1, 2025.
- [22] E. Shi *et al.*, “Joint AP-UE association and precoding for SIM-aided cell-free massive MIMO systems,” *IEEE Transactions on Wireless Communications*, vol. 24, no. 6, pp. 5352–5367, 2025.
- [23] Q. Li *et al.*, “Stacked intelligent metasurface-based transceiver design for near-field wideband systems,” *IEEE Transactions on Communications*, vol. 73, no. 9, pp. 8125–8139, 2025.
- [24] C. Liu *et al.*, “A programmable diffractive deep neural network based on a digital-coding metasurface array,” *Nature Electronics*, vol. 5, no. 2, pp. 113–122, 2022.
- [25] P. Liu *et al.*, “Full-range amplitude–phase metacells for sidelobe suppression of metalens antenna using prior-knowledge-guided deep-learning-enabled synthesis,” *IEEE Transactions on Antennas and Propagation*, vol. 71, no. 6, pp. 5036–5045, 2023.
- [26] L. Dong *et al.*, “Joint secure transmission enhancement of primary and secondary users in RIS aided spectrum sharing cognitive radio networks,” *IEEE Transactions on Cognitive Communications and Networking*, pp. 1–1, 2025.
- [27] J. Yuan *et al.*, “Intelligent reflecting surface-assisted cognitive radio system,” *IEEE Transactions on Communications*, vol. 69, no. 1, pp. 675–687, 2021.
- [28] C. Zhong *et al.*, “Deep reinforcement learning-based optimization for IRS-assisted cognitive radio systems,” *IEEE Transactions on Communications*, vol. 70, no. 6, pp. 3849–3864, 2022.
- [29] J. Ge *et al.*, “RIS-assisted cooperative spectrum sensing for cognitive radio networks,” *IEEE Transactions on Wireless Communications*, vol. 23, no. 9, pp. 12 547–12 562, 2024.
- [30] H. Hui *et al.*, “Robust beamforming design for RIS-assisted cognitive radio systems with hardware impairments,” *IEEE Transactions on Vehicular Technology*, vol. 73, no. 12, pp. 19 080–19 095, 2024.
- [31] B. Zhao *et al.*, “Robust beamforming for RIS enhanced transmissions in cognitive radio networks,” *IEEE Transactions on Vehicular Technology*, vol. 72, no. 5, pp. 6800–6804, 2023.
- [32] X. Wu *et al.*, “Robust secure transmission design for IRS-assisted mmwave cognitive radio networks,” *IEEE Transactions on Vehicular Technology*, vol. 71, no. 8, pp. 8441–8456, 2022.
- [33] Z. Wang *et al.*, “Multi-user ISAC through stacked intelligent metasurfaces: New algorithms and experiments,” in *GLOBECOM 2024 - 2024 IEEE Global Communications Conference*, 2024, pp. 4442–4447.
- [34] S. Li *et al.*, “Transmit beamforming design for ISAC with stacked intelligent metasurfaces,” *IEEE Transactions on Vehicular Technology*, vol. 74, no. 4, pp. 6767–6772, 2025.
- [35] Z. Li *et al.*, “Stacked intelligent metasurfaces-enhanced MIMO OFDM wideband communication systems,” *arXiv preprint arXiv:2503.00368*, 2025.
- [36] R. W. Heath *et al.*, “An overview of signal processing techniques for millimeter wave MIMO systems,” *IEEE Journal of Selected Topics in Signal Processing*, vol. 10, no. 3, pp. 436–453, 2016.
- [37] C. You *et al.*, “Wireless communication via double IRS: Channel estimation and passive beamforming designs,” *IEEE Wireless Communications Letters*, vol. 10, no. 2, pp. 431–435, 2021.
- [38] J. Chen *et al.*, “Low-complexity beamforming design for RIS-assisted fluid antenna systems,” in *2024 IEEE International Conference on Communications Workshops (ICC Workshops)*, 2024, pp. 1377–1382.
- [39] H. Chen *et al.*, “Multi-RIS-enabled 3D sidelink positioning,” *IEEE Transactions on Wireless Communications*, vol. 23, no. 8, pp. 8700–8716, 2024.
- [40] A. Fadakar *et al.*, “Hybrid codebook design for localization using electromagnetically reconfigurable fluid antenna system,” *arXiv preprint arXiv:2508.21351*, 2025.
- [41] G. H. Golub *et al.*, *Matrix computations*. JHU press, 2013.
- [42] J. An *et al.*, “Codebook-based solutions for reconfigurable intelligent surfaces and their open challenges,” *IEEE Wireless Communications*, vol. 31, no. 2, pp. 134–141, 2024.
- [43] K. M. Attiah *et al.*, “Beamforming design for integrated sensing and communications using uplink-downlink duality,” in *2024 IEEE International Symposium on Information Theory (ISIT)*, 2024, pp. 2808–2813.
- [44] S. Boyd, “Convex optimization,” *Cambridge UP*, 2004.
- [45] Y. Huang *et al.*, “Rank-constrained separable semidefinite programming with applications to optimal beamforming,” *IEEE Transactions on Signal Processing*, vol. 58, no. 2, pp. 664–678, 2010.